LA-UR-23-33548
Accepted Manuscript

Global Distribution of EMIC Waves and Its Association to Subauroral Proton Precipitation During the 27 May 2017 Storm: Modeling and Multipoint Observations

Shreedevi, P. R.; Yu, Yiqun; Miyoshi, Yoshizumi; Tian, Xingbin; Zhu, Minghui; Jordanova, Vania Koleva; Nakamura, S.; Jun, C-W; Kumar, Sandeep; Shiokawa, K.; Connors, Martin; Hori, T.; Shoji, M.; Shinohara, I.; Yokota, S.; Kasahara, S.; Keika, K.; Matsuoka, A.; Kadokura, A.; Tsuchiya, F.; Kumamoto, A.; et al.

To be published in: Journal of Geophysical Research: Space Physics

DOI to publisher's version: 10.1029/2023JA032337

Permalink to record:
https://permalink.lanl.gov/object/view?what=info:lanl-repo/lareport/LA-UR-23-33548

Global distribution of EMIC waves and its association to subauroral proton precipitation during the 27 May 2017 storm: Modeling and multipoint observations

P. R. Shreedevi[1,2], Yiqun Yu[2,3], Yoshizumi Miyoshi[1], Xingbin Tian [2], Minghui Zhu [2], Vania K. Jordanova [4], Satoko Nakamura [1], Chae-Woo Jun[1], Sandeep Kumar [1], Kazuo Shiokawa[1], Martin Connors [5], T. Hori [1], Masafumi Shoji [1], I. Shinohara [6], S. Yokota [7], S. Kasahara [8], K.Keika [8], A. Matsuoka [9], Akira Kadokura [10,11,12], Fuminori Tsuchiya [13], Atsushi Kumamoto [13], Yoshiya Kasahara [14]

[1]Institute for Space-Earth Environmental Research, Nagoya University, Japan
[2]School of Space and Environment, Beihang University, Beijing
[3]Key Laboratory of Space Environment Monitoring and Information Processing, Ministry of Industry and Information Technology, Beijing, China
[4]Space Science and Application, Los Alamos National Laboratory, Los Alamos, NM, United States
[5]Athabasca University, Canada
[6]ISAS/JAXA, Sagamihara, Japan
[7]Osaka University, Toyonaka, Japan
[8]University of Tokyo, Tokyo, Japan
[9]Kyoto University, Japan
[10]Polar Environment Data Science Center, ROIS-DS, Tokyo Japan
[11]National Institute of Polar Research, Tokyo Japan
[12]Polar Science Program, Graduate Institute for Advanced Studies, SOKENDAI, Tokyo, Japan
[13]Tohoku University, Japan
[14]Kanazawa University, Japan

Key Points:

- EMIC wave activity and proton precipitation were observed simultaneously in the dusk-midnight sector during the 27 May 2017 storm
- The BATSRUS+RAM-SCB model can capture the EMIC wave growth during the storm qualitatively

---

Corresponding author: P.R. Shreedevi, `shreedevipr@gmail.com`

- The EMIC wave scattering of ring current ions can account for the proton precipitation in the dusk-midnight sector during the storm

Abstract

Recent simulation studies using the RAM-SCB model showed that proton precipitation contributes significantly to the total energy flux deposited into the subauroral ionosphere thereby affecting the magnetosphere-ionosphere (MI) coupling. In this study, we use the BATS-R-US+RAM-SCB model to understand the evolution of ElectroMagnetic Ion Cyclotron (EMIC) waves in the inner magnetosphere, their correspondence to the proton precipitation into the subauroral ionosphere, and to assess the performance of the model in reproducing the EMIC wave-particle interactions. During the 27 May 2017 storm, Arase and RBSP-A satellites observed typical signatures of EMIC waves in the inner magnetosphere. Within this interval, DMSP and NOAA/MetOp satellites observed significant proton precipitation in the dusk-midnight sector. Simulation results show that H- and He-band EMIC waves are excited within regions of strong temperature anisotropy near the plasmapause. The simulated growth rates of EMIC waves show a similar trend to that of the EMIC wave power observed by the Arase and RBSP-A satellites, suggesting that the model can reproduce the EMIC wave activity qualitatively. The simulated H-band waves in the dusk sector are stronger than He-band waves possibly due to the presence of excess protons in the boundary conditions obtained from the BATS-R-US code. The precipitating proton fluxes reproduced by the simulation with EMIC waves are found to agree reasonably well with the DMSP and NOAA/MetOp satellite observations. It is suggested that EMIC wave scattering of ring current ions can account for proton precipitation observed by the DMSP and MetOp satellites during the 27 May 2017 storm.

1 Plain Language Summary

During geomagnetic storms, plasma waves are generated in the Earth's magnetosphere. Among these waves, ElectroMagnetic Ion Cyclotron (EMIC) waves can scatter protons from the ring current, causing them to precipitate into the subauroral ionosphere. Such precipitation not only affects the midlatitude ionosphere but also impacts the dynamics of the magnetosphere. Understanding the origin of magnetospheric plasma waves and how they interact with the magnetospheric populations, along with their subsequent impact on the ionosphere, is crucial for predicting space weather accurately. In our study, we combined ground and satellite observations with simulations using the BATS-R-US+RAM-SCB to investigate EMIC wave-particle interactions in the inner magnetosphere and the resulting proton precipitation during the May 27, 2017 storm. We found that EMIC waves

were excited in the dusk-midnight sector during the storm's main phase, within the regions of strong temperature anisotropy. The simulations reproduced the proton precipitation observed in the dusk-midnight sector by the DMSP/NOAA MetOP satellites fairly well. The model qualitatively captured the growth of the EMIC waves during the storm and showed that the EMIC waves, by scattering the ring current, were responsible for the proton precipitation into the dusk-midnight sector during the storm.

2 Introduction

Particle precipitation is a phenomenon unique to the high-latitude ionosphere that results from the dynamic coupling of the magnetosphere and the ionosphere. Depending on the solar wind driving conditions, several processes occur in the magnetosphere that can drive particle precipitation into the ionosphere and modulate the ionospheric electrodynamics [*Meredith et al.*, 2009; *Ni et al.*, 2012; *Xiao et al.*, 2013; *Yu et al.*, 2015; *Zhang et al.*, 2015; *Miyoshi et al.*, 2015a; *Shreedevi et al.*, 2016; *Kasahara*, 2018; *Shreedevi et al.*, 2019; *Miyoshi et al.*, 2020; *Fukizawa et al.*, 2020; *Zhu et al.*, 2021a]. The restructuring of the ionosphere due to particle precipitation can lead to disruption of the radio signals used for satellite navigation and communication [*Shreedevi et al.*, 2020; *Alfonsi*, 2022], and the field-aligned currents (FACs) carried by particle precipitation can cause geomagnetically induced currents capable of disrupting the electrically conducting technological systems in high latitude regions [*Ganushkina et al.*, 2017; *Gannon et al.*, 2019]. It can also affect the atmosphere's chemical composition and lead to ozone loss in the lower atmosphere [*Miyoshi et al.*, 2021; *Verronen et al.*, 2021]. Particle precipitation is, therefore, a major source of energy input into the high latitude ionosphere and has great impact on space weather.

Diffuse auroral precipitation is known to be the major contributor to the ionospheric energy budget, amounting to about 83%/71% of the total energy flux into the ionosphere during low/high solar wind driving conditions [*Newell et al.*, 2009]. Typically, the width of the diffuse aurora extends over 5°-10° in latitude and, when mapped along the magnetic field lines, traces to the magnetospheric regions extending from the ring current to the central plasma sheet [*Meredith et al.*, 2009; *Nishimura*, 2020]. Both electrons and protons contribute to the diffuse aurora with about 63%/21% and 57%/14% of the diffuse energy flux during periods of low/high geomagnetic activity [*Newell et al.*, 2009], suggesting that electron precipitation is the primary source of energy flux in the diffuse aurora. Studies of waves and precipitating fluxes have revealed that the most likely mechanism for the diffuse electron aurora is wave-particle interactions in the inner magnetosphere [*Meredith et al.*, 2009; *Miyoshi et al.*, 2015a], whereas that for the diffuse proton aurora it is the Field Line Curvature (FLC) scattering of inner magnetospheric protons [*Zhu et al.*, 2021a; *Yu et al.*, 2020]. Specifically, magnetospheric plasma waves such as whistler-mode chorus and electron cyclotron harmonic waves are effective in pitch angle scattering the electrons into the nightside ionosphere and causing the diffuse electron aurora [*Ni et al.*, 2008; *Meredith et al.*, 2009; *Miyoshi et al.*, 2015b, 2020; *Kasahara*, 2018; *Ozaki et al.*, 2019; *Fukizawa et al.*, 2020]. Within regions of L$\leq 8R_E$ in the inner magnetosphere, whistler-mode chorus waves are the dominant mechanism for precipitation loss of electrons [*Thorne*, 2010], while beyond L$=8R_E$, electron cyclotron harmonic waves are effective in producing the diffuse electron aurora [*Ni et al.*, 2012; *Zhang et al.*, 2015]. Additionally, the efficiency of diffuse auroral scattering by ECH waves might be significant in the inner magnetosphere, particularly around L$\sim 6R_E$ [*Ni et al.*, 2011; *Lou et al.*, 2021; *Fukizawa et al.*, 2022; *Yang et al.*, 2023].

Regions of intense proton precipitation where the precipitating proton energy flux exceeds that of electrons have been observed in the dusk-midnight sector at latitudes equatorward of the boundary of the diffuse auroral oval [*Lui et al.*, 1977; *Hardy et al.*, 1989; *Galand et al.*, 2001; *Yahnin and Demekhov*, 2018; *Semenova et al.*, 2019].*Tian et al.* [2020] assessed the correlation of energetic electron and proton precipitation boundaries with geomagnetic activity using the NOAA observations. They showed that the inner boundary of the 30-80 keV proton precipitation moves earthward during the storm's main phase and observed that the maximum precipitation flux in these regions is nearly one order of magnitude higher than that of the electrons. Based on the same datasets, *Ma et al.* [2022] established a model of isotropic boundary for 30-80 keV protons as a function of Kp indices, showing general variations of the latitudinal boundary of proton precipitation. The localized proton auroras, which are distinct regions visibly separated from the main auroral oval, and dominated by proton precipitation, typically appear in the dusk-midnight sector at lower magnetic latitudes during periods of intense geomagnetic activity [*Frey*, 2007]. The global images of the proton aurora by the IMAGE satellite showed that the detached subauroral proton aurora could be of a considerably large spatial and temporal extent [*Jordanova et al.*, 2007]. Magnetically conjugate observations of regions dominated by proton precipitation on the dayside have also been reported [*Immel et al.*, 2002]. Ground magnetic pulsations in the Pc1 and Pc5 range have been observed near the regions dominated by proton precipitation [*Mauk and McPherron*, 1980; *Yahnina et al.*, 2003; *Miyoshi et al.*, 2008].

Statistical/case studies using particle flux measurements show that the localized precipitation of ions in the subauroral region has a good correlation to the occurrence of EMIC waves in the inner magnetosphere [*Soraas et al.*, 1980, 1999; *Morley et al.*, 2009; *Ni et al.*, 2016; *Popova and Chernyaeva*, 2018; *Tian et al.*, 2023]. EMIC waves, usually classified as H-, He- and O-band waves originate near the earth's magnetic equator and propagate along magnetic field lines in the frequency range of 0.1-5 Hz. EMIC waves occur naturally from the temperature anisotropy of the medium energy ions (1-100keV) [*Cornwall*, 1965] and are observed during magnetically disturbed as well as quiet times [*Saikin et al.*, 2016]. Satellites have observed EMIC waves predominantly in the dusk-midnight and the prenoon sectors, with occurrence rates decreasing towards lower L shells [*Usanova et al.*, 2012; *Min et al.*, 2012; *Keika et al.*, 2013a; *Saikin et al.*, 2015]. The EMIC waves observed at lower L shells in the dusk-midnight sector are known to occur due to the fresh injections of plasma sheet ions into the ring current region during geomagnetic storms/substorms [*Jordanova et al.*, 2001; *Guan et al.*, 2020] ,whereas those observed at higher L shells in the prenoon sector are associated with compressions of the dayside magnetosphere due to fluctuations in the solar wind dynamic pressure [*McCollough et al.*, 2009; *Usanova et al.*, 2012; *Liu et al.*, 2019]. Theoretical calculations show that EMIC waves are easily excited in regions of enhanced cold plasma density and low magnetic field intensity in the equatorial plane [*Fraser et al.*, 1989; *Cornwall et al.*, 1970; *Hu et al.*, 1990; *Horne and Thorne*, 1993; *Jordanova et al.*, 2001]. The plasmapause and the plasmaspheric drainage plume are hence the regions where the convective growth rates of the EMIC waves are expected to be high [*Cornwall et al.*, 1970; *Fraser and Nguyen*, 2001].

Although both EMIC wave and FLC scattering contribute to the loss of magnetospheric ions, the majority of the precipitation loss due to scattering from EMIC waves occurs at lower L shells ($L \leq 4$), whereas that resulting from FLC scattering primarily occurs at higher L shells ($L > 4$-5) [*Zhu et al.*, 2021a; *Yu et al.*, 2020]. *Jordanova et al.* [1997, 2006] calculated self-consistently the generation of He-band EMIC waves by anisotropic ring current ions with the Ring current Atmosphere interactions Model with Self-consistent Magnetic field (RAM-SCB). They showed that the pitch-angle scattering of the ring current ions with the He-band EMIC waves led to significant proton precipitation within regions of enhanced wave excitation in the dusk sector, followed by pitch angle isotropization and reduction of further wave growth. *Shreedevi et al.* [2021] implemented a statistical model of both H- and He-band EMIC waves in the RAM-SCB model and found that including H-band waves in the

RAM-SCB model led to better agreement with the ion flux measurements from the DMSP and NOAA satellites. *Zhu et al.* [2021a] investigated the relative contributions of FLC and EMIC wave scattering to the energetic ion precipitation using the RAM-SCB model. They found that the ionospheric conductance due to the proton precipitation associated with FLC scattering has a negligible influence on the electric potential. On the contrary, the ionospheric conductance in the dusk-midnight sector is greatly enhanced due to the EMIC wave-induced proton precipitation and has a significant influence on the electric potential in the dusk sector. *Tian et al.* [2022], using the simulations of the RAM-SCB model coupled with the GLOW model, showed that E-region conductivity and ionospheric electron density in the dusk-midnight sector is amplified by the EMIC wave-induced precipitation of tens of keV of protons, further leading to enhancement of the integrated auroral conductance.

As described, particle precipitation is an important link between the magnetosphere and the ionosphere and an essential component of space weather. To obtain realistic predictions of the global patterns of ionospheric conductivity and the ionospheric electric potential, which are key variables that determine space weather, it is necessary to accurately represent the mechanisms responsible for particle precipitation in modeling it. Over the past decade, significant improvements have been made to the RAM-SCB model [*Jordanova et al.*, 2022] and the role of wave-particle interaction and FLC scattering in precipitation loss into the ionosphere has been demonstrated using global simulations and ground/satellite-based observations [*Jordanova et al.*, 1996, 2001; *Yu et al.*, 2020; *Tian et al.*, 2022; *Shreedevi et al.*, 2021; *Zhu et al.*, 2021a]. Most of these simulation studies focused on understanding the ionospheric response in terms of ion and electron precipitation, and the resulting changes in global conductivity and electric potential. It is, however, difficult to fully verify the mechanisms for the evolution of EMIC waves in the inner magnetosphere and associated ionospheric effects using either modelling or observational studies alone. To verify the mechanisms for the temporal and spatial evolution of EMIC wave activity in the inner magnetosphere and its relation to the ion precipitation at subauroral latitudes, simulation studies combining simultaneous measurements of the local conditions in the inner magnetosphere and the ionosphere are essential. Hence in this study we simulate the evolution of EMIC waves and proton precipitation during storm time using the Block-Adaptive-Tree Solar-Wind Roe-Type Upwind Scheme (BATS–R–US)+RAM-SCB model and compare it with observations (1) to understand the causative mechanisms responsible for the temporal and spatial evolution of EMIC wave activity and proton precipitation into the subauroral latitudes, and (2) to assess the performance of the BATS–R–US+RAM-SCB model in reproducing the EMIC wave-particle interactions. Comparison of the BATS-R-US+RAM-SCB simulations with the in situ measurements from Arase, RBSP-A, DMSP, NOAA MetOp satellites and ground magnetometers will provide insight into the mechanisms responsible for the EMIC wave generation as well as the resulting particle precipitation and be helpful in prediction of space weather effects in the ionosphere.

3 Satellite/ground-based observations

The onset and evolution of the geomagnetic storm event of 27-28 May 2017 is studied using the solar wind and geomagnetic parameters measured by the ACE/WIND satellites. These data are available on the OMNIWeb database and the World Data Center, Kyoto, respectively.

The particle precipitation into the ionosphere is studied using the in situ measurements from the Defense Meteorological Satellite Program (DMSP) and the National Oceanic and Atmospheric Administration (NOAA) Meteorological Operational satellite (MetOp) 01 and 02 satellites. The DMSP satellite is a polar sun-synchronous satellite orbiting at an altitude of ∼840 km with an orbital period of ∼101 minutes. We use the in situ particle fluxes in the energy range 30eV-30keV measured in 1-sec cadences by the Special Sensor J/4 (SSJ/4) instrument onboard the DMSP satellites. The NOAA MetOp satellites are also sun-synchronous polar orbiting satellites with an orbital period of ∼102 minutes. The NOAA MetOp satellites carry the Medium Energy Proton and Electron Detector (MEPED) instrument, which includes a set of two particle detectors oriented in 0° and 90° directions. These detectors provide proton flux measurements in six energy bands and have information about precipitating and geomagnetically trapped particles, respectively. In this study, we use the 30-80 keV proton fluxes provided by both detectors at 16-sec cadences.

The Arase satellite traverses the inner magnetosphere with an orbital inclination of ∼31° and provides in situ measurements of particle fluxes and wave activity along its orbits [*Miyoshi et al.*, 2018a]. We used the Magnetic Field Experiment (MGF) on board the Arase satellite [*Matsuoka*, 2018; *Miyoshi et al.*, 2018a] to measure the EMIC wave activity in the inner magnetosphere. To understand the dynamics of energetic ion fluxes in the inner magnetosphere, we studied the H^+, He^+ and O^+ fluxes in the medium energy range of 10-180 keV/q obtained by the medium-energy particle experiments-ion mass analyzer (MEP-i) instrument [*Yokota*, 2017; *Miyoshi et al.*, 2018a] onboard the Arase satellite. The ambient electron density in the inner magnetosphere was derived using the upper hybrid resonance deduced from the high-frequency analyser (HFA) of the Plasma Wave Experiment (PWE) [*Kasahara*, 2018; *Kumamoto et al.*, 2018].

The Van Allen Probes (Radiation Belt Storm Probes (RBSP)) [*Mauk*, 2013] also provides information about the EMIC wave activity and the variability in the hot and cold particle fluxes in the inner magnetosphere. RBSP is composed of two identical satellites orbiting near the equatorial plane. In this study, we use observations only from the RBSP-A satellite. The EMIC wave activity in the inner magnetosphere was analysed using the tri-axial fluxgate magnetometer (MAG), which is a part of the Electric and Magnetic Field Instrument Suite and Integrated Science (EMFISIS) [*Kletzing*, 2013] instrument onboard the RBSP-A. The cold electron densities in the inner magnetosphere are derived using the high-frequency receiver (HFR), which is also a part of EMFISIS. The variations in the situ ion fluxes in the inner magnetosphere in the energy range of 1-50 keV are studied using the H^+, He^+ and O^+ fluxes obtained by the Helium, Oxygen, Proton and Electron (HOPE) [*Funsten*, 2013] instrument. The HOPE instrument is a part of the energetic particle, composition, and thermal plasma suite (ECT) [*Spence*, 2013].

Information about the Pc1 wave activity at midlatitude stations Pinawa (PINA) and Thief River Falls (THRF) used in this study is obtained from the CARISMA (Canadian Array for Realtime Investigations of Magnetic Activity) chain of ground-based magnetometers [*Mann et al.*, 2008].

4 Model Description

The RAM-SCB model computes the temporal evolution of the phase space distribution function F_l in the presence of electric and magnetic field self-consistently by coupling the RAM code with a 3D force-equilibrium model of the magnetic field (SCB) model and an electric field (RIM) model [*Jordanova et al.*, 2006, 2010; *Zaharia et al.*, 2006; *Yu et al.*, 2017]. In the RAM-SCB model, the Ring current Atmosphere interactions Model (RAM) code determines the kinetic physics of the major species in the inner magnetosphere, i.e. H^+, He^+, O^+ and electrons for all magnetic local times at L shells ranging from 2 to 6.5 R_E by solving the bounce-averaged kinetic equation given by:

$$\begin{aligned}\frac{\partial F_l(t,R_o,\phi,E,\alpha)}{\partial t} + \frac{1}{R^2}\frac{\partial}{\partial R_o}(R_o^2\langle\frac{dR_o}{dt}\rangle F_l) + \frac{\partial}{\partial\phi}(\langle\frac{d\phi}{dt}\rangle F_l) \\ + \frac{1}{\gamma p}\frac{\partial}{\partial E}(\gamma p\langle\frac{dE}{dt}\rangle F_l) + \frac{1}{h\mu_o}\frac{\partial}{\partial\mu_o}(h\mu_o\langle\frac{d\mu_o}{dt}\rangle F_l) \\ = \langle(\frac{\partial F_l}{\partial t})_{loss}\rangle\end{aligned} \tag{1}$$

where

R_o is the radial distance in the magnetic equatorial plane,

E is the kinetic energy of the particle, which varies from 0.15 keV to 400 keV,

μ_o is the cosine of the equatorial pitch angle α_o, α varies from 0 to 90° ,

ϕ is the geomagnetic east longitude,

p is the relativistic momentum of the particle,

γ is the Lorentz factor,

$h(\mu_o)$ is proportional to the bounce path length in the magnetic field.

The three critical inputs needed to drive the RAM code are the time-dependent plasma conditions at the boundary of the model i.e., 6.5 R_E, and the electric and magnetic field. The magnetic field required in the RAM code is obtained from a 3D force-balanced equilibrium model of the earth's magnetic field. The coupling of the RAM code with the 3D force-equilibrium model of the magnetic field (B) is achieved using an iterative approach. Every 5 minutes, the parallel and perpendicular plasma pressure distributions in the equatorial plane estimated by the RAM code are provided to the 3D force-equilibrium code to arrive at the force balance satisfying

$$J \times B = \nabla \cdot P \tag{2}$$

where J is the current density, and P is the pressure tensor.
The magnetic field calculated in the 3D equilibrium code is passed back to the RAM where it is used to evolve self-consistently the ring current particle distributions.

The plasma boundary conditions at $6.5R_E$, i.e. the outer boundary of the RAM code, are obtained from the BATS-R-US (MHD code). We used the Space Weather Modeling Framework (SWMF) to facilitate the two-way coupling of the RAM-SCB code with the MHD code. The satellite measurements of the upstream solar wind conditions, time-shifted to 32 R_E are used to drive the MHD code. The MHD code calculates the plasma conditions at geosynchronous orbit, which is then passed on to the RAM-SCB model as its boundary condition. The RAM-SCB model uses the plasma boundary conditions to estimate the plasma pressure in the inner magnetosphere. The two-way coupling of the RAM-SCB with the MHD model also allows the MHD model to use the total plasma pressure calculated by the RAM-SCB to correct the MHD solution.

The electric field needed in the RAM code is obtained from the RIM model. The RIM model is a two-dimensional height-integrated ionospheric potential solver which calculates the ionospheric electric potential by solving the Poisson's equation:

$$\nabla \cdot (\Sigma \cdot \nabla \phi) = -J_{\parallel} \sin I \tag{3}$$

where $J_{\parallel}$ is the field-aligned current (FAC), Σ is the height-integrated ionospheric conductance tensor, and I is the inclination angle of the magnetic field. The RIM model is two-way coupled to the RAM-SCB model through the SWMF. The FACs and the ionospheric conductance at 100 km are needed to drive the RIM model. The FACs near the inner boundary of the MHD model are passed on to the RIM to solve for the ionospheric electric potential. The convection electric potential from the RIM model is then mapped to the equatorial plane of the RAM code along the SCB magnetic field lines and used to calculate the E×B drift velocity there. More details on the integration of the RAM-SCB model into the SWMF can be found elsewhere [*Welling et al.*, 2018; *Jordanova et al.*, 2022].

The plasma injected into the nightside boundary of the RAM-SCB model drifts through the ring current region under the influence of the electric and magnetic field and undergoes various loss and acceleration processes. The dominant loss processes for the electrons and ions in the inner magnetosphere are included in the RAM-SCB model. The electron loss processes incorporated in the model include pitch angle scattering of electrons by whistler-mode chorus waves and hiss waves. The ion loss processes included in the model are charge exchange with neutral hydrogen, EMIC wave-particle scattering and the precipitation resulting from the widening of the loss cone as the particles are convected from higher to lower L shells.

The resonant interaction between ring current protons and EMIC waves induces particle diffusion affecting both pitch-angle and energy. However, it is evident from studies such as *Lyons* [1974] and *Jordanova et al.* [1998] that energy diffusion is weaker than pitch-angle diffusion. The cross-diffusion terms can also become important for EMIC wave-particle interactions [*Xiao et al.*, 2009; *Su et al.*, 2011]. Specifically, *Lyons* [1974] demonstrated that the pitch-angle diffusion coefficient ($D_{\alpha\alpha}$) is approximately 1-2 orders of magnitude higher than the energy diffusion coefficient, while *Jordanova et al.* [1998] highlighted that pitch-angle diffusion is more effective than energy diffusion for the ring current ions. Hence, EMIC wave-particle interaction is considered as a particle diffusion in pitch angle in the RAM-SCB model. The diffusion equations for the loss associated with the pitch angle scattering is

$$\langle (\frac{\partial F_l}{\partial t}) \rangle = \frac{1}{h\mu_o} \frac{\partial}{\partial \mu_o} \left[h\mu_o \langle D_{\mu_o\mu_o} \rangle \frac{\partial F_l}{\partial \mu_o} \right] \tag{4}$$

$$\langle D_{\mu_o\mu_o} \rangle = (1 - \mu_o^2) \langle D_{\alpha\alpha} \rangle \tag{5}$$

where $\langle D_{\alpha\alpha}(E, \alpha) \rangle$ is the bounce averaged pitch angle diffusion coefficient associated with wave-particle interactions obtained from the quasi-linear theory. The bounce-averaged diffusion coefficients $D_{\alpha\alpha}$ as a function of (f_{pe}/f_{ce}, L, MLT, E, α) are obtained using the Full Diffusion Code (FDC) [*Ni et al.*, 2015, 2018; *Cao et al.*, 2016] for different f_{pe}/f_{ce} grids ranging from 2 to 20 and L shells in the RAM domain. The diffusion coefficients are then scaled to the local EMIC wave amplitude as $D_{\alpha\alpha} * {B_w}^2$ and interpolated into the model grids. The EMIC wave amplitudes needed to calculate the quasi-linear diffusion coefficients are obtained from the EMIC wave amplitude model statistically derived from Van Allen Probes measurements [*Saikin et al.*, 2016]. The statistical EMIC model based on *Saikin et al.* [2016] has a resolution of ΔL=0.25 and ΔMLT=3. More details on the implementation of the EMIC wave model into the RAM-SCB can be found in *Shreedevi et al.* [2021].

5 Proton precipitation and EMIC wave activity: Observations

Figure 1(a-f) shows the solar wind (at the nose of the bow shock) and geomagnetic conditions during the 27 May 2017 storm. A sudden enhancement in the solar wind speed, density and pressure can be seen at ∼1540 UT on 27 May 2017, which indicates the arrival of an interplanetary shock at the magnetopause, driven by a coronal mass ejection (CME). Later, at ∼1930 UT, the z-component of the interplanetary magnetic field (IMF B_z) turned southward, initiating the main phase of the geomagnetic storm. The Dst index, after steadily decreasing for about 10 hours, reached a minimum value of -125 nT at ∼0710 UT on 28 May 2017. Several strong fluctuations in the AL index (panel (f)) during the entire main phase of the storm (∼ 10 hours) indicates the development of substorm currents and significant energy input into the MI system.

In order to understand the evolution of particle precipitation into the ionosphere during the main phase of the 27 May 2017 storm, the particle flux measurements from the DMSP and NOAA/MetOp 01 and 02 satellites were examined. Figure 2(a,b) shows a comparison of the 30-80 keV proton fluxes and the 30-100 keV electron fluxes measured by the 0° and 90° telescopes onboard MetOp 02 and 01 satellites, respectively. In Figure 2(a,b), the green and blue dots represent the proton and electron fluxes observed by the 0° telescope, respectively, while the black and pink dots represent those observed by the 90° telescope, respectively. The 0° telescopes measure the field-aligned precipitating fluxes, whereas the 90° telescopes measure geomagnetically trapped particles. As seen, during 2205-2220 UT, the MetOp 02 satellite located at the $\sim$21 MLT sector observed a large enhancement in the 30-80 keV precipitating proton fluxes at L $\sim$ 4.75-6.5 Re. Later, during 2305-2315 UT, the MetOp 01 satellite detected significant enhancements in the 30-80 keV precipitating proton fluxes at L$\sim$3.5-6.5 Re in the midnight sector. The precipitating proton fluxes observed by both satellites are higher than the electron fluxes by about an order of magnitude. Previous reports of similar observations suggest that such enhancements in the precipitating proton fluxes in the dusk-to-midnight sector could result from EMIC wave-particle interactions [*Tian et al.*, 2022, and references therein].

Similarly, Figure 2(c,d) shows a comparison of <30 keV proton and electron fluxes observed by the DMSP F16 satellite. As seen, the DMSP F16 satellite was located in the dusk MLT sector during the main phase of the storm, where it observed enhanced precipitation of protons as well as electrons. The observations indicate that in the $\sim$19 MLT sector, the electron precipitation primarily occurred at high latitudes, while the proton precipitation extended beyond the boundary of electron aurora (-58.7° MLAT), reaching subauroral latitudes up to $\sim$-56.3° MLAT. Such precipitation of protons in the dusk sector in a region equatorward of the electron aurora can be a source of E-region electron density/conductivity enhancements in the midlatitude ionosphere [*Tian et al.*, 2020], and is generally attributed not to FLC scattering but to the presence of EMIC waves [*Semenova et al.*, 2019].

To verify the presence of EMIC wave activity in the inner magnetosphere at locations where the proton precipitation was observed, we examined the Arase and RBSP-A satellite measurements. The Arase satellite was located in the midnight MLT sector close to the magnetic equator (MLAT$\sim$2°N) during 2200-2400 UT on 27 May 2017. Figure 3(a) shows power spectral density (PSD) of the wave magnetic field as observed by the Arase satellite during 2145-2240 UT on 27 May 2017. The white lines represent the local H^+, He^+ and O^+

ion gyrofrequencies, respectively. Around ∼2215-2230 UT, the magnetic pulsations are seen to enhance greatly below the He+ local gyrofrequency suggesting the presence of He-band EMIC waves in the midnight MLT sector. In the dusk MLT sector, the RBSP-A satellite flew close to the magnetic equator during 2200-2400 UT on 27 May 2017 . Figure 3(b) shows the wave power spectral density observed by the RBSP-A satellite during 2200-2400 UT. Evidently, there are significant enhancements in the power spectral density near the local He+ ion gyrofrequency starting at 2230 UT. These observations therefore provide evidence for the presence of He-band EMIC wave activity in the dusk and midnight MLT sector during 2200-2400 UT on 27 May 2017.

EMIC waves were also detected on the ground by induction coil magnetometers at midlatitude stations during the main phase of the storm on 27 May 2017. Figure 3(c-d) shows the evolution of the power spectral density of geomagnetic pulsation starting 2000 UT on 27 May 2017 up to 0100 UT on 28 May 2017 at Pinawa (PINA) and Thief River Falls (THRF), respectively. Both stations detected the presence of Pc1 pulsations during 2000-2200 UT, which is likely to be EMIC waves that have propagated from the magnetosphere. These wave excitations, although weaker in wave power, were probably in response to the sudden enhancements in the solar wind dynamic pressure (see Figure 1(d)). Later, after ∼2230 UT, there is a significant enhancement in the EMIC wave activity at PINA and THRF stations. The EMIC wave pulsations at both stations exhibit similar features and are seen to continue until 0100 UT on 28 May 2017.

To put in context the observations of the subauroral proton precipitation and EMIC wave activity, the location of the DMSP, NOAA MetOp, Arase and RBSP-A satellites and the ground magnetometers (PINA, THRF) from 2200 UT on 27 May to 0100 UT on 28 May are shown in the L-MLT plane in Figure 3(e). Clearly, the DMSP F16 satellite flew close to the dusk sector at ∼00:09 UT on 28 May. Notably, the two ground magnetometer stations, PINA and THRF, are located in the dusk sector during 2230-0100 UT, close to the DMSP F16 and RBSP-A locations. The RBSP-A satellite and the ground magnetometers at PINA and THRF detected EMIC waves during 2230-0100 UT, suggesting that the EMIC wave activity was prevalent in the dusk sector during this interval. Hence, the subauroral proton precipitation detected by the DMSP F16 satellite is most likely related to the EMIC wave activity in the dusk sector. Similarly, the orbit of MetOp 02 satellite is close to the Arase satellite in the midnight sector, as seen in Figure 3(e). This again suggests that the significant enhancements in the precipitating proton fluxes observed by the MetOp 02 satellite (at ∼2215 UT) could be related to the presence of EMIC waves in the midnight sector observed by the Arase satellite at ∼2215 UT. The MetOp 01 satellite is also located in the midnight sector on 27 May. However, simultaneous observations of EMIC waves were not available from locations close to MetOp 01 satellite which recorded proton flux enhancements at ∼2305 UT. To verify the mechanisms for the evolution of EMIC waves in the dusk-midnight MLT sector and the associated ionospheric proton precipitation, we simulated the wave-particle interactions during the 27-28 May 2017 geomagnetic storm using the BATSRUS+RAM-SCB model with and without EMIC waves. The simulation results are described in the following section.

6 Temporal and spatial evolution of EMIC waves: Simulation results

We simulated the EMIC wave-particle interactions in the inner magnetosphere during the geomagnetic storm of 27 May 2017 using the BATSRUS+RAM-SCB model. To understand the growth and evolution of the EMIC waves in the simulation, we calculated the linear convective growth rates for parallel propagating H-, He- and O- band EMIC waves following the method described by *Kozyra et al.* [1984]; *Jordanova et al.* [2003]; *Fok et al.* [2016]; *Zhu et al.* [2021b]. We used the distributions of the H^+, He^+ and O^+ ions simulated with EMIC waves to calculate the linear convective growth rate given by

$$S = \frac{\epsilon}{V_g} \tag{6}$$

where ϵ is the temporal growth rate, and V_g is the wave group velocity.

The temporal growth rate is given by:

$$\begin{aligned}\epsilon = \frac{\omega_i}{\Omega_p} = \frac{\pi^2\Omega_p^2}{n_{wp}Xk}&\left[\sum_l \frac{1}{M_l^2}\int\left(\frac{\partial f_{wl}}{\partial v_\perp} + \frac{M_l}{\Omega_p}kv_\perp\frac{\partial f}{\partial v_\parallel}\right)_{v_\parallel = u_r} v_\perp^2 dv_\perp\right] \\ &\cdot\left[\frac{(1+\frac{n_{cp}}{n_{wp}})(2-X)}{(1-X)^2} + \sum_{l>p}\frac{n_{wl}+n_{cl}}{n_{wp}}\frac{M_l(2-XM_l)}{(1-XM_l)^2}\right]^{-1}\end{aligned} \tag{7}$$

The group velocity V_g is given by:

$$\begin{aligned}V_g = \frac{\partial\omega_r}{\partial k} = \frac{2\Omega_p c}{\omega_{wpp}}&\left[\frac{(1+\frac{n_{cp}}{n_{wp}})}{1-X} + \sum_{l>p}\frac{n_{wl}+n_{cl}}{n_{wp}}\frac{M_l}{1-XM_l}\right]^{\frac{1}{2}} \\ &\cdot\left[\frac{(1+\frac{n_{cp}}{n_{wp}})(2-X)}{(1-X)^2} + \sum_{l>p}\frac{n_{wl}+n_{cl}}{n_{wp}}\frac{M_l(2-XM_l)}{(1-XM_l)^2}\right]^{-1}\end{aligned} \tag{8}$$

where $n_{w(c)l}$ is the warm(cold) ion density of species l,

k is the wave number,

X = ω_r/Ω_p ,

M_l is the atomic number of species l,

f_{wl} is the phase density of warm ion species l,

ω_{wpp} is the warm proton plasma frequency, and

u_r is the parallel resonance velocity: $u_r = \frac{\Omega_p(XM_l-1)}{kM_l}$

Figure 4(a) shows the global distribution of the maximum convective growth rate of H-, He- and O-band EMIC waves at 2215 UT. The H-, He- and O- band EMIC waves are seen to appear in the dusk-to-midnight sector. The H-band EMIC wave is strongest among the three bands, with significant wave growth at L=4-6 Re in the afternoon-to-dusk sector. The He-band wave is seen to appear around L=3-6 Re in the midnight-to-dusk sector but is weaker in magnitude and spatial extent compared to the H-band EMIC wave. The O-band EMIC wave, however, is confined to a very narrow region beyond L>6 Re in the dusk sector and has an insignificant growth rate compared to the other two EMIC wave bands. Statistical study of EMIC wave occurrence by *Saikin et al.* [2015] also suggests that the H- and He-band EMIC waves can occur at all MLTs within the L shell region of L=2-6.5 Re.

EMIC wave excitation is known to arise naturally from the temperature anisotropy of the magnetospheric proton populations [*Kennel and Petschek*, 1966]. The hot anisotropic plasma necessary for the EMIC wave generation is supplied from the plasma sheet during periods of enhanced magnetospheric convection, while the cold, dense plasmaspheric plume supports the wave growth through changes of the resonance energy [*Jordanova et al.*, 2001]. To understand the EMIC wave growth in the simulation, we examined the simulated local plasma conditions and the associated temperature anisotropy. Figure 4(b) shows the distribution of the ring current ions species H^+, He^+ and O^+ of energy E=40 keV and pitch angle=90° at 2215 UT. The three hot ring current ions are seen to be distributed in the midnight-to-afternoon sector. This is because the ions in this energy range, injected into the inner magnetosphere during periods of strong convection, drift in the westward direction. All three hot ion species have peaks in the pre-midnight sector, with protons having the largest fluxes, followed by oxygen and helium ions. In situ observations and statistical studies have shown that the protons usually dominate the ring current during geomagnetic storms, whereas the He^+ ions have the lowest density [*Ebihara*, 2011]. As for the O^+ ions, their fluxes in the ring current are observed to increase during storm time and may rise to levels comparable to the proton fluxes [*Keika et al.*, 2013b; *Kistler et al.*, 2016]. These features are also evident in the simulated hot ion distribution.

The temperature anisotropy associated with the hot H^+, He^+ and O^+ ions are shown in Figure 4(c). It is defined as

$$A = \frac{T_\perp}{T_\parallel} - 1 \tag{9}$$

where A is the anisotropy, and $T_\perp$ and $T_\parallel$ are the temperature of the respective ion species, perpendicular and parallel to the magnetic field. The anisotropy parameter A shown in Figure 4(c) is calculated for all energies ranging from 0.15-400 keV. It is observed to be greater than zero across a broader region, particularly at L<6 Re, implying that the ring current is unstable within these regions. Hence, we expect EMIC waves to be excited in this broad region. However, the high growth rate regions for the three EMIC wave bands are mostly confined to the regions in the vicinity of the plasmapause in the midnight-to-dusk sector. This could be because, in addition to the ion anisotropy, the growth of the EMIC waves in the inner magnetosphere is also influenced by factors including the cold plasma densities and the local magnetic field [*Kozyra et al.*, 1984; *He et al.*, 2017]. Figure 4(d) shows the simulated densities of the cold H^+, He^+ and O^+ ions at 2215 UT and the plasmaspheric boundary marked using the black dots. Following *Jordanova et al.* [1997], we assumed the cold ion composition ratios to be $[H^+, He^+, O^+] = [0.77, 0.20, 0.03]$ in the simulation, which is clearly reflected in the distribution of cold ion densities shown in Figure 4(d). It is seen that in response to the enhanced magnetospheric convection (IMF B_z <-15 nT) at 2215 UT, there is significant erosion of the nightside plasmasphere and the plasmapause in the nightside is shrunk to regions closer to the earth L=4 Re. Evidently, the regions of enhanced maximum growth rates of H-, He- and O- band waves (Figure 4(a)) coincide with the region where the hot ring current ions overlap with the plasmapause. Since the cold background plasma can influence the dispersion relation and provide suitable conditions for the growth of the EMIC waves [*Kozyra et al.*, 1984; *Usanova et al.*, 2016], the simulated wave growth, as expected, is maximum in these regions.

7 Temporal and spatial evolution of EMIC waves: Data-model comparison

To investigate if the BATSRUS+RAM-SCB simulation reproduces reasonably well the temporal and spatial evolution of the regions of EMIC instability, we compared the observed EMIC wave power with the simulated linear growth rates. It is to be noted that the growth of the linear instability to observable wave power depends also on the wave propagation, amplification, saturation and damping which are not considered here. Since the linear wave growth indicates a region of potential wave growth, we only make qualitative comparisons of the EMIC wave power with the simulated linear growth rates. The temporal variation of the integrated wave power estimated from the Arase and RBSP-A satellite observations is shown in Figure 5(a,c). The blue line shown in Figure 5(a,c) represents the integrated wave power between fc_{He}-fc_O where fc_{He} and fc_O are the He^+ and O^+ local gyrofrequencies, respectively. It can be seen from Figure 5(a,c) that the He-band integrated wave power increases significantly at the Arase satellite location at ∼2215 UT in the midnight MLT sector and at the RBSP-A satellite location at ∼2245-2320 UT in the dusk MLT sector, respectively. This is because the Arase and RBSP-A satellites passed through regions of intense He-band EMIC wave activity (see Figure 3) during this interval. The He-band waves are, therefore predominant in the dusk and midnight sector during the main phase of the 27 May geomagnetic storm.

Figure 5(b) shows the simulated linear growth rates at the Arase location in the midnight sector. Starting at 2200 UT, there is an increase in both the simulated H- and He-band growth rate along the Arase orbit. It is seen that the He-band wave growth rate steadily increases until 2215 UT but drops to a low value after this period. Figure 4(a) however shows that the dusk-to-midnight sector is the favorable region for He-band wave growth. Evidently, the growth rates distributed in an azimuthally elongated region along the plasmapause (Figure 4(a)) are stronger towards the dusk MLTs. The sudden drop in the He-band wave growth could therefore be because the orbit of the Arase satellite is outside the region of the strong EMIC wave growth (after 2215 UT).

Similarly, in Figure 5(d), the simulated linear growth rates along the RBSP-A satellite in the dusk sector are presented. It is evident that the growth rate of He-band EMIC waves in the dusk sector increased during periods where the integrated wave power of the He-band wave is also enhanced. Later, after ∼2310UT, the growth rate of the simulated He-band wave is seen to drop in a similar trend as the RBSP-A observed He-band wave power. The He-band growth rates exhibit a rather broad peak although the observations show several fluctuations in the wave power. Such a broad peak in the linear growth rate could be a result of the wide grid resolution of the statistical EMIC wave model ($\Delta\mathrm{L} = 0.25$ and $\Delta\mathrm{MLT} = 3$). The smoothing out of small-scale variations could also be a result of the averaging across numerous events in the statistical EMIC wave model. Furthermore, the finer structures in the observed EMIC wave pulsations may not be accurately represented in our study, as the simulation does not incorporate the evolution of EMIC waves due to factors such as wave propagation, amplification, saturation and other non-linear effects. It is to be noted that in contrast to the absence of clear signatures of strong H-band EMIC waves in the observations, the simulated linear growth rates of H-band waves is high in the dusk sector.

Basically, the growth and amplification of the EMIC wave require the hot anisotropic ring current ion species to spatially overlap with the cold, dense plasmaspheric populations [*Cornwall*, 1965; *Kennel and Petschek*, 1966; *Jordanova et al.*, 2001; *Thorne*, 2010]. In addition, any variations in the cold plasma density, cold/warm ion composition, including the minor heavy ion species helium and oxygen found in the ring current during the stormtime, can strongly influence the growth of the EMIC wave bands and their cut-off frequencies [*Fraser*, 1985; *Kozyra et al.*, 1984; *Jordanova et al.*, 1997]. Hence, to understand the discrepancies in the temporal and spatial evolution of the simulated EMIC wave growth rates, we compared the simulated background plasma conditions in the midnight (Arase satellite location) and dusk sector (RBSP-A satellite location) with the in situ observations. Figure 6 shows the comparison of the 10-180 keV H^+, He^+ and O^+ ion fluxes in the premidnight sector measured by the MEP-i instrument onboard the Arase satellite with the simulated ion fluxes during 1900-2400 UT on 27 May 2017. Figure 6(a,c,e) show that several hot ions are injected into the nightside magnetosphere due to enhanced magnetospheric convection caused by the southward turning of IMF at ∼2100 UT on 27 May 2017. The intensity of the modelled proton, helium and oxygen fluxes (Figure 6(b,d,f)) show overall agreement with the in situ observations. There is, however the presence of large ion fluxes (∼10-50 keV) at the beginning of the storm, i.e. at ∼2100-2200 UT in the simulation. The simulated and observed cold electron density along the Arase satellite orbit is shown in Figure 6(g). It can be seen that the RAM-SCB model captures the evolution of the cold electron density in the midnight sector very well.

Similarly, Figure 7 shows the comparison of the 1-50 keV fluxes in the dusk sector obtained from the ECT/HOPE instrument onboard the RBSP-A satellite with the ion spectrogram obtained from the simulation with EMIC waves. It can be seen that the RBSP-A satellite located in the dusk sector observed particle injections starting ∼2030 UT. The intensity of the modelled proton fluxes shows better agreement with the RBSP-A observations. But, there seems to be a significant overestimation of the modelled He^+ and O^+ ion fluxes, mainly in the lower energies and before 2230 UT. The simulated low energy (1-10 keV) He^+ and O^+ ion fluxes are about two orders of magnitude higher than the observed fluxes in the dusk sector. Figure 7(g) shows the comparison of the observed and simulated cold densities along the RBSP-A orbit. Clearly, the simulated cold electron density in the dusk sector is in good agreement with the RBSP-A observations.

As described, the modelled cold electron densities at the Arase (midnight sector) and RBSP-A (dusk sector) locations match well with the in situ observations. However, the cold ion composition ratios assumed to be $[H^+, He^+, O^+]=[0.77, 0.20, 0.03]$ in the calculation of the growth rates, may not represent the realistic background conditions in the inner magnetosphere. Previous studies have shown that even a small increase in the ratio of the hot to cold ion densities can severely influence the propagation or amplification of the EMIC waves [*Kozyra et al.*, 1984]. We however do not have direct measurements of the composition of the cold background heavy ions at the Arase and RBSP-A locations, and so this may add some ambiguity to the growth rate calculations. Apart from this, there are also some discrepancies in the spatial and temporal evolution of the simulated hot ion fluxes as compared to the in situ observations, which may affect the growth and propagation of the simulated EMIC waves. The presence of large modelled fluxes along both the Arase (Figure 6) and RBSP-A (Figure 7) orbits at the beginning of the storm is because the RAM-SCB model uses the boundary conditions from the BATSRUS MHD code which may be overestimating the magnitude of plasma convected from the nightside. There is also significant overestimation of the simulated He^+ and O^+ ion fluxes in the dusk sector, especially the lower energies. Since the convective growth rates are calculated under the assumption of the linear theory, the growth rates due to the multi ion populations is determined by the superposition of the growth or damping rates of each individual ions in the ring current. *Jordanova et al.* [1996]; *Jordanova* [2011], using the RAM-SCB model showed that the presence of larger fluxes of both He^+ and O^+ ions contributes negatively to the growth rate of the He-band wave. Similarly, *Henning and Mace* [2014] investigated the effect of the relative abundance of the H^+, He^+ and O^+ ions in the ring current on the growth and damping of the three EMIC wave bands by numerically solving the dispersion relation for parallel propagating EMIC waves in a multicomponent plasma. They showed that (1) the larger the proton fluxes in the ring current, the lower the cutoff frequency of the H-band branch, resulting in a positive contribution to the H-band growth rate, and (2) an increase in the percentage of hot O^+ ions contribute to an increase in the growth of the H- and O-band EMIC wave, while the He-band EMIC waves undergoes damping.

In the simulation, the linear growth rates of the He-band EMIC waves along the Arase and RBSP satellite orbit show a similar trend as the observed integrated wave power albeit the broad peaks in the growth rates. There is however significant growth of H-band EMIC waves in contrast to the observations. The notable overestimation of the heavy ion fluxes at the satellite locations (Figure 6 and 7), suggests that the boundary conditions from the BATSRUS MHD code do not accurately represent the realistic conditions in the dusk sector. The appearance of such larger fluxes at L shells closer to earth (L $\sim$ 4) has been observed in previous simulations also [*Yu et al.*, 2015, 2017], and, could be a result of an initial condition with excess protons or an overly injection due to large electric field. There is strong growth of the H-band waves along the satellite orbits in the simulation, probably due to the presence of large H^+ ion fluxes in the dusk sector. Furthermore, the presence of the large O^+ ion fluxes suppress the simulated growth rate of the He-band wave at the satellite locations in the dusk sector. Considering these differences, we suggest that the model can capture the linear growth of the He-band EMIC waves at the satellite locations qualitatively.

8 Proton precipitation: Data-Model comparisons

Figure 8(a-d) shows the low (E=1 keV) and moderate (E=40keV) energy proton precipitation into the ionosphere at 2215 UT on 27 May 2017, as obtained from the BATSRUS+RAM-SCB simulations with and without EMIC waves. The plasmapause boundary defined as the location where the electron density in the plasmasphere falls below 50/cc is shown using the black dots in Figure 8(a-d). The plasmapsheric electron densities were calculated using the plasmasphere model by *Rasmussen et al.* [1993]. A comparison of the precipitating fluxes from the two simulations shows that the ionospheric proton precipitation increases significantly in the presence of EMIC waves. The precipitating fluxes are seen to increase mainly in the midnight-to-dusk sector. These locations are also consistent with the in situ observations shown in Figure 2 where proton precipitation and EMIC wave activity enhanced over a wide range of L shells in the dusk-midnight sector during the main phase of the 27 May storm.

As for the EMIC waves in the simulation, the global distribution of H- and He-band EMIC wave intensities at 2215 UT is shown in Figure 8(e,f). It is seen that the H- and He-band EMIC waves have the highest intensities in the noon to dusk sector. These intensities are based on the statistical studies of EMIC wave properties [*Saikin et al.*, 2016], which show that the noon-to-dusk sector is the preferred location for the occurrence of peak intensities of both the H- and He-band EMIC wave activity. The precipitation loss of ring current protons into the ionosphere occurs due to its gyroresonant interaction with EMIC waves [*Jordanova et al.*, 2001]. The rate at which the protons are scattered by the H- and He-band EMIC waves are represented using the diffusion coefficients. Figure 8(g-h) shows the diffusion coefficients ($D_{\alpha\alpha}$) at E=40 keV and pitch angle=53° for the H- and He-band EMIC waves. The diffusion coefficients associated with the H-band waves are seen to enhance over all MLT sectors, with peak values over a narrow range of L-shells (L=3-5 Re) in the dusk sector and at L=3-6 Re in the pre-noon sector. The diffusion coefficients due to the He-band waves are seen to be high in the noon to premidnight sector, over a wide range of L shells (L=2.5-6.5 Re) where the He-band EMIC wave intensities are also higher. Clearly, (1) the precipitation of low energy proton fluxes in the midnight/morning sector (where the diffusion coefficients due to He-band are very low) occurs mainly due to the scattering of protons by the H-band waves, and (2) the precipitating proton fluxes of high energy observed in the noon-to-midnight sector (where the diffusion coefficients due to He-band are high) are mainly contributed by the He-band waves.

To evaluate if the model is able to reproduce the realistic proton precipitation into the ionosphere during the 27 May storm, we compared the simulated precipitating proton fluxes with the NOAA MetOp and DMSP observations. Figure 9(a,b) shows the comparison of the NOAA/MetOp 02 and 01 observations with the simulated 30-80 keV precipitating proton fluxes. While the 0 deg telescope onboard the NOAA MetOp satellites measures the field aligned fluxes around 840 km, the two simulations provide the precipitating fluxes within the loss cones at 200 km. We directly compare the simulated precipitating fluxes with the NOAA MetOp observations because the difference in loss cones between these two altitudes is very small. In Figure 9(a,b), the gold line represents the 30-80 keV proton fluxes measured by the 0 deg telescope, whereas the black and purple dots represent the 30-80 keV proton fluxes obtained from the simulations with and without EMIC waves respectively. It is seen that at around 2215 UT, the MetOp 02 satellite located in the premidnight sector (~21.4 MLT) observed a large increase in the 30-80 keV precipitating proton fluxes at ~55-60° latitude. Later at around 2310 UT, the MetOp 01 satellite flew in the premidnight sector (~21.7 MLT) where it observed a significant increase in the 30-80 keV precipitating proton fluxes at ~51-70° latitude. In the simulations without EMIC waves, only weak enhancements in the precipitating fluxes are produced. There is a substantial difference of over two orders of magnitude between the observations and the fluxes simulated without EMIC waves. The simulations with EMIC waves, however, reproduce the 30-80 keV ion precipitation observed by the NOAA MetOp satellites fairly well.

Recently, *Ni et al.* [2023] utilized RBSP-B and NOAA data, to develop a model linking the EMIC wave-driven proton diffusion to the ratio of precipitated-to-trapped proton count rates, enabling the inference of EMIC wave intensity needed to cause the observed proton precipitation. Their model's estimation of EMIC wave intensity closely matched the actual observations of EMIC waves, falling within a range of 1.5 times the observed values. Our study's NOAA MetOp observations, shown in Figure 3 also indicate high ratios of precipitated-to-trapped proton fluxes, suggesting significant pitch-angle diffusion into the loss cone. Moreover, the pitch-angle diffusion coefficients estimated by *Ni et al.* [2023] are similar to those in our study, and are considered sufficient to explain the observed proton precipitation. These findings further affirm the significant role of EMIC waves in driving the observed proton precipitation during the 27 May 2017 storm. With event-specific wave observations and associated wave-particle interactions, the diffusion coefficients can be more realistic and the agreement on the precipitation flux may be even better [*Yu et al.*, 2022].

Figure 10 shows the comparison of the <30keV ion energy spectrogram and integrated ion energy flux obtained from the DMSP F16 satellite with the BATSRUS+RAM-SCB simulations with and without EMIC waves. The different panels in Figure 10 show (a) the <30 keV ion energy flux measured by the DMSP F16 satellite, (b)-(c) simulated energy flux and (d) the integrated ion energy flux from DMSP F16 observations and the simulations with and without EMIC waves. In the simulation with EMIC waves, there is significant precipitating proton flux in the subauroral regions, whose intensities agree reasonably well with the DMSP observations. As for the case without EMIC waves, there is little or no precipitating proton flux in the subauroral regions. The comparison among the integrated ion energy fluxes from the DMSP observations and the two simulations shown in Figure 10(d) also presents a similar scenario. The integrated ion energy flux from the simulations with EMIC waves is seen to match well with the DMSP observations. The integrated ion energy flux from the simulation without EMIC waves is much lower in magnitude and not comparable with the DMSP observations.

It may be noted that the localized enhancements in the proton precipitation and the low latitude boundary of the precipitating fluxes is not captured well by the model. This maybe due to the larger grid resolution of the statistical EMIC wave model. The EMIC waves observed by the Arase and RBSP-A satellite are bursty and confined to certain L shells as seen in Figure 3. On the other hand, the EMIC wave amplitudes in the statistical wave model are distributed over wider L and MLT ranges i.e., ΔL = 0.25 and ΔMLT = 3 hour as seen in Figure 8(e,f). The localized proton enhancements may not be reproduced by the RAM-SCB model as the wider grid resolution in the statistical EMIC wave leads to a latitudinally wide region of proton precipitation. Even so, the RAM-SCB simulation with EMIC waves is able to reproduce the proton precipitation into the subauroral ionosphere observed by the DMSP and NOAA MetOp satellites during the 27 May 2017 storm reasonably well. This also highlights the need to develop a more self-consistent EMIC wave model with higher spatial and temporal resolution.

9 Summary and Conclusions

Proton precipitation, through its control over the ionospheric conductances, can modulate the midlatitude ionospheric dynamics and play a significant role in determining the extent of energy transfer between the magnetosphere and ionosphere [*Ridley et al.*, 2004; *Zhu et al.*, 2021a]. *Jordanova et al.* [1997, 2006], using the RAM-SCB model, showed that the gyroresonant interaction of the EMIC waves with the ring current ions is an important mechanism that can lead to precipitation loss of ions into the ionosphere. Realistic predictions of the ionospheric dynamics, therefore, require an accurate representation of the EMIC wave-particle interactions in space weather models. Although previous studies using the RAM-SCB model have discussed the role of EMIC wave-particle interaction in precipitation loss of ions into the ionosphere, they mainly focussed on how the proton precipitation affects the ionospheric conductivity and the subsequent effects on the MI coupling dynamics. The spatial and temporal evolution of the modelled precipitation, its association with the time and location of the EMIC wave excitation, and its relation to the local plasma conditions in the inner magnetosphere needs further verification with situ observations. In this study, we simulated the geomagnetic storm of 27 May 2017 and examined the evolution of the proton precipitation into the ionosphere and its relation to the EMIC wave activity in the inner magnetosphere using simulations of the BATSRUS+RAM-SCB model (with and without EMIC waves) and the DMSP, NOAA MetOp, Arase, RBSP-A and ground magnetometer measurements. The main results from this study are as follows:

1. At ~2215-2230 UT on 27 May 2017, the Arase satellite, located in the midnight MLT sector, close to the magnetic equator, observed He-band EMIC waves at L shells ~4.5-4.9

Re. Within this interval, the MetOp 02 satellite located close to the Arase satellite observed an increase in the 30-80 keV precipitating proton fluxes, which could be a result of the EMIC wave activity in the midnight sector. Later, at ∼2230-2400 UT on 27 May 2017, the RBSP-A satellite flying near the magnetic equator in the dusk MLT sector observed intense He-band EMIC wave activity at L shells ∼4.65-5.4 Re. The DMSP F16 satellite located in the dusk sector measured significant enhancements in the <30 keV proton precipitation at ∼0007 UT on 28 May. Although not an exact conjunction event, it is likely that the EMIC wave-particle interactions observed by the RBSP-A satellite at the magnetic equator led to the proton precipitation observed by the DMSP satellite. The predominance of EMIC wave activity at wider L shells in the dusk sector was further confirmed by the ground magnetometer observations from PINA and THRF stations.

2. In the simulation, the preferred region for the occurrence of the H-, He- and O-band EMIC waves is the dusk-to-midnight sector. This is consistent with our understanding that the dusk-to-midnight sector, where the hot anisotropic ring current ions spatially overlap the cold dense plasmaspheric populations, is the preferred region for the excitation and growth of EMIC waves [*Jordanova et al.*, 2001].

3. Variations in the integrated wave power of the He-band EMIC waves estimated from the Arase and RBSP-A satellite measurements suggest that the He-band EMIC waves were predominant in the dusk/midnight sector during the main phase of the storm. However, in the simulation, the H-band waves were found to be predominant at the RBSP-A location in the dusk sector. Nevertheless, at the Arase/RBSP-A satellite location in the midnight/dusk sector, the He-band EMIC waves show positive linear growth rates and a similar trend as the observed EMIC wave power. Hence, it is suggested that the model can capture the linear growth of the He-band EMIC waves at the satellite locations qualitatively.

4. The simulation reproduces the cold electron density at the Arase and RBSP-A satellite locations very well, but there are some discrepancies in the modelled ion fluxes, especially at the location of the RBSP-A satellite in the dusk sector. The overestimation of the modeled ion fluxes in the dusk sector is because the boundary conditions during the stormtime obtained from the BATSRUS MHD code do not represent the realistic conditions at 6.5 Re, i.e. the boundary of the RAM-SCB model. The large enhancements in the H^+ ions in the dusk sector lead to the positive growth rates of the H-band EMIC waves [*Henning and Mace*, 2014]. The significant damping of the He-band EMIC wave in the

simulation is because the He-band EMIC wave growth is very sensitive to the presence of O^+ ions [*Kozyra et al.*, 1984; *Jordanova et al.*, 2001; *Henning and Mace*, 2014]. The discrepancies in the boundary conditions obtained from the BATSRUS MHD code contribute to the overestimation of the hot ion fluxes in the dusk sector, resulting in the significant growth/damping of the H/He-band EMIC waves in the dusk sector during the main phase of the 27 May 2017 storm.

5. In the absence of EMIC wave scattering, there is little or no proton precipitation at the DMSP and NOAA MetOp satellite locations. However, the $<$30 keV precipitating proton fluxes obtained from the simulation with EMIC waves agree reasonably well with the DMSP F16 measurements from the dusk sector. Similarly, the 30-80 keV precipitating proton fluxes from the simulation with EMIC waves show good agreement with the NOAA MetOp observations from the midnight sector.

6. The DMSP, NOAA MetOp, RBSP-A and Arase satellite observations suggest a good correspondence between the occurrence of proton precipitation and the EMIC wave activity in the dusk-midnight sector. The RAM-SCB model can capture the proton precipitation into the ionosphere and the EMIC wave activity in the inner magnetosphere reasonably well. Hence, it is suggested that the EMIC wave-particle interactions in the dusk-midnight sector gave rise to the proton precipitation into the subauroral latitudes during the main phase of the 27 May 2017 storm.

Since the simulation does not calculate the EMIC wave growth rates self consistently, subsequent effects such as the reduction of proton anisotropy in the ring current as the EMIC wave grows and its resulting impact on the EMIC wave dynamics are not included. Similarly, the wave propagation and other non-linear effects are not taken into account in the model. More investigations using satellite-based initial and boundary conditions are necessary to assess how the contributions from the effects mentioned above, can improve the EMIC growth rate calculations in the model. This will be a part of our future studies. Nonetheless, the comparison of the simulated/observed proton precipitation, EMIC wave activity and local plasma conditions in this study provides evidence of the role of EMIC wave scattering in the evolution of proton precipitation during the 27 May storm.

10 Open Research

Arase satellite datasets used in this study are available in these in-text data citation references: *Miyoshi et al.* [2018a], *Miyoshi et al.* [2018b], *Matsuoka and Imajo* [2018], *Kasahara et al.* [2021], *Yokota et al.* [2019], *Miyoshi and Jun* [2018] obtained from the ERG Science Center operated by the ISAS/JAXA and ISEE/Nagoya University (https://ergsc.isee.nagoya-u.ac.jp/index.shtml). Science data of the ERG (Arase) satellite in the present study analyzed MGF Lv.2 high-resolution magnetic field data (https://doi.org/10.34515/DATA.ERG-06000), HFA Lv.3 electron density data (https://doi.org/10.34515/DATA.ERG-10001), MEP-i Lv.2 omniflux data (https://doi.org/10.34515/DATA.ERG-03001), and Orbit L3 v02 data (https://doi.org/10.34515/DATA.ERG-12001). The RBSP-A data used in this study are publicly available at https://rbsp-ect.newmexicoconsortium.org/data_pub/. Van Allen Probes EMFISIS data are available at https://emfisis.physics.uiowa.edu/data/index. The CARISMA magnetometer data are publicly available at https://www.carisma.ca/carisma-data-repository. The simulation data for this research are available at https://doi.org/10.5281/zenodo.10258540 [*P R and Yu*, 2023] . Solar wind and geomagnetic indices are provided by http://cdaweb.gsfc.nasa.gov. NOAA MetOp data and the DMSP data are available at http://satdat.ngdc.noaa.gov/sem/poes/ and http://www.ngdc.noaa.gov/stp/satellite/dmsp/.

Acknowledgments

This work is supported by the JSPS-grants 22F22022, 22K21345, 23H01129, 22F22329. Work at Los Alamos was conducted under the auspices of the U. S. Department of Energy with partial support from NSF Award IAA2027951. RAM-SCB model is available at https://github.com/lanl/RAM-SCB. The simulations were performed on TianHe-2 at National Supercomputer Center in Guangzhou, China. The authors thank I.R. Mann, D.K. Milling and the rest of the CARISMA team for data. CARISMA is operated by the University of Alberta, funded by the Canadian Space Agency.

References

Alfonsi, B. N. C. P. e. a., L. (2022), Review of environmental monitoring by means of radio waves in the polar regions: From atmosphere to geospace, *Surveys in Geophysics*, *43*, 1609–1698, doi:https://doi.org/10.1007/s10712-022-09734-z.

Cao, X., B. Ni, J. Liang, Z. Xiang, Q. Wang, R. Shi, X. Gu, C. Zhou, Z. Zhao, S. Fu, and J. Liu (2016), Resonant scattering of central plasma sheet protons by multiband

EMIC waves and resultant proton loss timescales, *Journal of Geophysical Research: Space Physics*, *121*(2), 1219–1232, doi:https://doi.org/10.1002/2015JA021933.

Cornwall, J. M. (1965), Cyclotron instabilities and electromagnetic emission in the ultra low frequency and very low frequency ranges, *Journal of Geophysical Research (1896-1977)*, *70*(1), 61–69, doi:10.1029/JZ070i001p00061.

Cornwall, J. M., F. V. Coroniti, and R. M. Thorne (1970), Turbulent loss of ring current protons, *Journal of Geophysical Research (1896-1977)*, *75*(25), 4699–4709, doi:10.1029/JA075i025p04699.

Ebihara, Y., Y.and Miyoshi (2011), *Dynamic Inner Magnetosphere: A Tutorial and Recent Advances*, pp. 145–187, Springer Netherlands, Dordrecht, doi:$10.1007/978 - 94 - 007 - 0501 - 2_9$.

Fok, M.-C., G. V. Khazanov, E. N. Krivorutsky, and A. Glocer (2016), Convective growth of electromagnetic ion cyclotron waves from realistic ring current ion distributions, *Journal of Geophysical Research: Space Physics*, *121*(11), 10,966–10,977, doi:https://doi.org/10.1002/2016JA022964.

Fraser, B. (1985), Observations of ion cyclotron waves near synchronous orbit and on the ground, *Space Science Reviews*, *42*(1572-9672), doi:10.1007/BF00214993.

Fraser, B., and T. Nguyen (2001), Is the plasmapause a preferred source region of electromagnetic ion cyclotron waves in the magnetosphere?, *Journal of Atmospheric and Solar-Terrestrial Physics*, *63*(11), 1225–1247, doi:https://doi.org/10.1016/S1364-6826(00)00225-X.

Fraser, B. J., W. J. Kemp, and D. J. Webster (1989), Ground-satellite study of a Pc1 ion cyclotron wave event, *Journal of Geophysical Research: Space Physics*, *94*(A9), 11,855–11,863, doi:https://doi.org/10.1029/JA094iA09p11855.

Frey, H. U. (2007), Localized aurora beyond the auroral oval, *Reviews of Geophysics*, *45*(1), doi:10.1029/2005RG000174.

Fukizawa, M., T. Sakanoi, Y. Miyoshi, Y. Kazama, Y. Katoh, Y. Kasahara, S. Matsuda, A. Matsuoka, S. Kurita, M. Shoji, M. Teramoto, S. Imajo, I. Sinohara, S.-Y. Wang, S. W.-Y. Tam, T.-F. Chang, B.-J. Wang, and C.-W. Jun (2020), Pitch-angle scattering of inner magnetospheric electrons caused by ECH waves obtained with the Arase satellite, *Geophysical Research Letters*, *47*(23), e2020GL089,926, doi:https://doi.org/10.1029/2020GL089926.

Fukizawa, M., T. Sakanoi, Y. Miyoshi, Y. Kazama, Y. Katoh, Y. Kasahara, S. Matsuda, A. Kumamoto, F. Tsuchiya, A. Matsuoka, S. Kurita, S. Nakamura, M. Shoji, M. Teramoto, S. Imajo, I. Shinohara, S.-Y. Wang, S. W.-Y. Tam, T.-F. Chang, B.-J. Wang, and C.-W. Jun (2022), Statistical study of approaching strong diffusion of low-energy electrons by chorus and ECH waves based on in situ observations, *Journal of Geophysical Research: Space Physics*, *127*(3), e2022JA030,269, doi: https://doi.org/10.1029/2022JA030269, e2022JA030269 2022JA030269.

Funsten, S.-R. G. A. e. a., H.O. (2013), Helium, oxygen, proton, and electron (HOPE) mass spectrometer for the radiation belt storm probes mission, *Space Science Reviews*, *179*, 423–484, doi:https://doi.org/10.1007/s11214-013-9968-7.

Galand, M., T. Fuller-Rowell, and M. Codrescu (2001), Response of the upper atmosphere to auroral proton, *J. Geophys. Res. Space Physics*, *106*, 127.

Gannon, J. L., A. Swidinsky, and Z. Xu (2019), *Geomagnetically induced currents from the Sun to the power grid*, Wiley Online Library.

Ganushkina, N., A. Jaynes, and M. Liemohn (2017), Space weather effects produced by the ring current particles, *Surveys in Geophysics*, *212*, 1315–1344, doi: https://doi.org/10.1007/s11214-017-0412-2.

Guan, C., X. Shang, Y. Xie, C. Yang, S. Zhang, S. Liu, and F. Xiao (2020), Generation of simultaneous h+ and he+ band emic waves in the nightside radiation belt, *Science China Technological Sciences*, *63*, 2369–2374, doi:10.1007/s11431-019-1545-6.

Hardy, D. A., M. S. Gussenhoven, and D. Brautigam (1989), A statistical model of auroral ion precipitation, *Journal of Geophysical Research: Space Physics*, *94*(A1), 370–392, doi: 10.1029/JA094iA01p00370.

He, Z., L. Chen, H. Zhu, Z. Xia, G. D. Reeves, Y. Xiong, L. Xie, and Y. Cao (2017), Multiple-satellite observation of magnetic dip event during the substorm on 10 october 2013, *Geophysical Research Letters*, *44*(18), 9167–9175, doi: https://doi.org/10.1002/2017GL074869.

Henning, F. D., and R. L. Mace (2014), Effects of ion abundances on electromagnetic ion cyclotron wave growth rate in the vicinity of the plasmapause, *Physics of Plasmas*, *21*(4), 042,905, doi:10.1063/1.4873375.

Horne, R. B., and R. M. Thorne (1993), On the preferred source location for the convective amplification of ion cyclotron waves, *Journal of Geophysical Research: Space Physics*, *98*(A6), 9233–9247, doi:10.1029/92JA02972.

Hu, Y. D., B. J. Fraser, and J. V. Olson (1990), Amplification of electromagnetic ion cyclotron waves along a wave path in the earth's multicomponent magnetosphere, *Geophysical Research Letters*, *17*(8), 1053–1056, doi:https://doi.org/10.1029/GL017i008p01053.

Immel, T. J., S. B. Mende, H. U. Frey, L. M. Peticolas, C. W. Carlson, J.-C. Gérard, B. Hubert, S. A. Fuselier, and J. L. Burch (2002), Precipitation of auroral protons in detached arcs, *Geophysical Research Letters*, *29*(11), 14–1–14–4, doi: https://doi.org/10.1029/2001GL013847.

Jordanova, V., S. Morley, M. Engel, H. Godinez, K. Yakymenko, M. Henderson, Y. Yu, and Y. Miyoshi (2022), The RAM-SCB model and its applications to advance space weather forecasting, *Advances in Space Research*, doi:https://doi.org/10.1016/j.asr.2022.08.077.

Jordanova, V. K. (2011), *Self-Consistent Simulations of Plasma Waves and Their Effects on Energetic Particles*, pp. 189–199, Springer Netherlands, Dordrecht, doi: https://doi.org/10.1007/$978 - 94 - 007 - 0501 - 2_10$.

Jordanova, V. K., J. U. Kozyra, and A. F. Nagy (1996), Effects of heavy ions on the quasi-linear diffusion coefficients from resonant interactions with electromagnetic ion cyclotron waves, *Journal of Geophysical Research: Space Physics*, *101*(A9), 19,771–19,778, doi: 10.1029/96JA01641.

Jordanova, V. K., J. U. Kozyra, A. F. Nagy, and G. V. Khazanov (1997), Kinetic model of the ring current-atmosphere interactions, *Journal of Geophysical Research: Space Physics*, *102*(A7), 14,279–14,291, doi:10.1029/96JA03699.

Jordanova, V. K., C. J. Farrugia, J. M. Quinn, R. M. Thorne, K. E. Ogilvie, R. P. Lepping, G. Lu, A. J. Lazarus, M. F. Thomsen, and R. D. Belian (1998), Effect of wave-particle interactions on ring current evolution for January 10–11, 1997: Initial results, *Geophysical Research Letters*, *25*(15), 2971–2974, doi:10.1029/98GL00649.

Jordanova, V. K., C. J. Farrugia, R. M. Thorne, G. V. Khazanov, G. D. Reeves, and M. F. Thomsen (2001), Modeling ring current proton precipitation by electromagnetic ion cyclotron waves during the May 14–16, 1997, storm, *Journal of Geophysical Research: Space Physics*, *106*(A1), 7–22, doi:10.1029/2000JA002008.

Jordanova, V. K., A. Boonsiriseth, R. M. Thorne, and Y. Dotan (2003), Ring current asymmetry from global simulations using a high-resolution electric field model, *Journal of Geophysical Research: Space Physics*, *108*(A12), doi:https://doi.org/10.1029/2003JA009993.

Jordanova, V. K., Y. S. Miyoshi, S. Zaharia, M. F. Thomsen, G. D. Reeves, D. S. Evans, C. G. Mouikis, and J. F. Fennell (2006), Kinetic simulations of ring current evolution during the Geospace Environment Modeling challenge events, *Journal of Geophysical Research: Space Physics*, *111*(A11), doi:10.1029/2006JA011644, a11S10.

Jordanova, V. K., M. Spasojevic, and M. F. Thomsen (2007), Modeling the electromagnetic ion cyclotron wave-induced formation of detached subauroral proton arcs, *Journal of Geophysical Research: Space Physics*, *112*(A8), doi:10.1029/2006JA012215.

Jordanova, V. K., S. Zaharia, and D. T. Welling (2010), Comparative study of ring current development using empirical, dipolar, and self-consistent magnetic field simulations, *Journal of Geophysical Research: Space Physics*, *115*(A12), doi:10.1029/2010JA015671, a00J11.

Kasahara, K.-Y. K. H. e. a., Y. (2018), The plasma wave experiment (PWE) on board the Arase (ERG) satellite, *Earth Planets Space*, *70*, 86, doi:https://doi.org/10.1186/s40623-018-0842-4.

Kasahara, Y., A. Kumamoto, F. Tsuchiya, H. Kojima, S. Matsuda, A. Matsuoka, M. Teramoto, M. Shoji, S. Nakamura, M. Kitahara, Y. Miyoshi, and I. Shinohara (2021), Exploration of energization and Radiation in Geospace (ERG) Plasma Wave Experiment (PWE) High Frequency Analyzer (HFA) Level-3 electron density data [Dataset], ERG Science Center, Institute for Space-Earth Environmental Research, Nagoya University, doi:10.34515/DATA.ERG-10001.

Keika, K., K. Takahashi, A. Y. Ukhorskiy, and Y. Miyoshi (2013a), Global characteristics of electromagnetic ion cyclotron waves: Occurrence rate and its storm dependence, *Journal of Geophysical Research: Space Physics*, *118*(7), 4135–4150, doi: https://doi.org/10.1002/jgra.50385.

Keika, K., L. M. Kistler, and P. C. Brandt (2013b), Energization of O+ ions in the earth's inner magnetosphere and the effects on ring current buildup: A review of previous observations and possible mechanisms, *Journal of Geophysical Research: Space Physics*, *118*(7), 4441–4464, doi:https://doi.org/10.1002/jgra.50371.

Kennel, C. F., and H. E. Petschek (1966), Limit on stably trapped particle fluxes, *Journal of Geophysical Research (1896-1977)*, *71*(1), 1–28, doi: https://doi.org/10.1029/JZ071i001p00001.

Kistler, L. M., C. G. Mouikis, H. E. Spence, A. M. Menz, R. M. Skoug, H. O. Funsten, B. A. Larsen, D. G. Mitchell, M. Gkioulidou, J. R. Wygant, and L. J. Lanzerotti (2016), The source of O+ in the storm time ring current, *Journal of Geophysical Research: Space Physics*, *121*(6), 5333–5349, doi:https://doi.org/10.1002/2015JA022204.

Kletzing, K.-W. A. M. e. a., C.A. (2013), The electric and magnetic field instrument suite and integrated science (EMFISIS) on rbsp, *Space Science Reviews*, *179*, 127–181, doi: https://doi.org/10.1007/s11214-013-9993-6.

Kozyra, J. U., T. E. Cravens, A. F. Nagy, E. G. Fontheim, and R. S. B. Ong (1984), Effects of energetic heavy ions on electromagnetic ion cyclotron wave generation in the plasmapause region, *Journal of Geophysical Research: Space Physics*, *89*(A4), 2217–2233, doi:https://doi.org/10.1029/JA089iA04p02217.

Kumamoto, A., F. Tsuchiya, Y. Kasahara, Y. Kasaba, H. Kojima, S. Yagitani, K. Ishisaka, T. Imachi, M. Ozaki, S. Matsuda, M. Shoji, A. Matsuoka, Y. Katoh, Y. Miyoshi, and T. Obara (2018), High frequency analyzer (HFA) of plasma wave experiment (PWE) onboard the arase spacecraft, *Earth, Planets and Space*, *70*(1880-5981), 82, doi: https://doi.org/10.1186/s40623-018-0854-0.

Liu, S., Z. Xia, L. Chen, Y. Liu, Z. Liao, and H. Zhu (2019), Magnetospheric multiscale observation of quasiperiodic emic waves associated with enhanced solar wind pressure, *Geophysical Research Letters*, *46*(13), 7096–7104, doi: https://doi.org/10.1029/2019GL083421.

Lou, Y., X. Cao, B. Ni, W. Tu, X. Gu, S. Fu, Z. Xiang, and X. Ma (2021), Diffuse auroral electron scattering by electrostatic electron cyclotron harmonic waves in the dayside magnetosphere, *Geophysical Research Letters*, *48*(5), e2020GL092,208, doi: https://doi.org/10.1029/2020GL092208, e2020GL092208 2020GL092208.

Lui, A. T. Y., D. Venkatesan, C. D. Anger, S. I. Akasofu, W. J. Heikkila, J. D. Winningham, and J. R. Burrows (1977), Simultaneous observations of particle precipitations and auroral emissions by the ISIS 2 satellite in the 19–24 MLT sector, *Journal of Geophysical Research (1896-1977)*, *82*(16), 2210–2226, doi:10.1029/JA082i016p02210.

Lyons, L. R. (1974), Pitch angle and energy diffusion coefficients from resonant interactions with ion–cyclotron and whistler waves, *Journal of Plasma Physics*, *12*(3), 417–432, doi: 10.1017/S002237780002537X.

Ma, L., Y. Yu, X. Tian, and J. Cao (2022), An Empirical Model of the Proton Isotropic Boundary (IB), *Journal of Geophysical Research: Space Physics*, *127*(9), e2022JA030,843, doi:https://doi.org/10.1029/2022JA030843, e2022JA030843 2022JA030843.

Mann, I., D. Milling, I. Rae, L. Ozeke, A. Kale, Z. Kale, K. Murphy, A. Parent, M. Usanova, D. Pahud, E.-A. Lee, V. Amalraj, D. Wallis, V. Angelopoulos, K.-H. G. C. Russell, H.-U. Auster, and H. Singerg (2008), The upgraded CARISMA magnetometer array in the THEMIS era, *Space Science Reviews*, *141*, 413–451, doi: https://doi.org/10.1007/s11214-008-9457-6.

Matsuoka, A., and S. Imajo (2018), Exploration of energization and Radiation in Geospace (ERG) Magnetic Field Experiment (MGF) Level-2 high-resolution (64/128/256 hz) magnetic field data [Dataset], ERG Science Center, Institute for Space-Earth Environmental Research, Nagoya University, doi:10.34515/DATA.ERG-06000.

Matsuoka, T. M. N. R. e. a., A. (2018), The Arase (ERG) magnetic field investigation, *Earth Planets Space*, *70*, 43, doi:https://doi.org/10.1186/s40623-018-0800-1.

Mauk, B. H., and R. L. McPherron (1980), An experimental test of the electromagnetic ion cyclotron instability within the earth's magnetosphere, *The Physics of Fluids*, *23*(10), 2111–2127, doi:10.1063/1.862873.

Mauk, F. N. K. S. e. a., B.H. (2013), Science objectives and rationale for the radiation belt storm probes mission, *Space Science Reviews*, *179*, 3–27, doi: https://doi.org/10.1007/s11214-012-9908-y.

McCollough, J. P., S. R. Elkington, and D. N. Baker (2009), Modeling emic wave growth during the compression event of 29 june 2007, *Geophysical Research Letters*, *36*(18), doi: https://doi.org/10.1029/2009GL039985.

Meredith, N. P., R. B. Horne, R. M. Thorne, and R. R. Anderson (2009), Survey of upper band chorus and ECH waves: Implications for the diffuse aurora, *Journal of Geophysical Research: Space Physics*, *114*(A7), doi:https://doi.org/10.1029/2009JA014230.

Min, K., J. Lee, K. Keika, and W. Li (2012), Global distribution of EMIC waves derived from THEMIS observations, *Journal of Geophysical Research: Space Physics*, *117*(A5), doi:https://doi.org/10.1029/2012JA017515.

Miyoshi, Y., and C.-W. Jun (2018), Exploration of energization and Radiation in Geospace (ERG) Orbit Level-3 data [Dataset], ERG Science Center, Institute for Space-Earth Environmental Research, Nagoya University, doi:10.34515/DATA.ERG-12001.

Miyoshi, Y., K. Sakaguchi, K. Shiokawa, D. Evans, J. Albert, M. Connors, and V. Jordanova (2008), Precipitation of radiation belt electrons by EMIC waves, observed from ground and space, *Geophysical Research Letters*, *35*(23), doi:https://doi.org/10.1029/2008GL035727.

Miyoshi, Y., S. Oyama, S. Saito, S. Kurita, H. Fujiwara, R. Kataoka, Y. Ebihara, C. Kletzing, G. Reeves, O. Santolik, M. Clilverd, C. J. Rodger, E. Turunen, and F. Tsuchiya (2015a), Energetic electron precipitation associated with pulsating aurora: EISCAT and Van Allen Probe observations, *Journal of Geophysical Research: Space Physics*, *120*(4), 2754–2766, doi:https://doi.org/10.1002/2014JA020690.

Miyoshi, Y., S. Saito, K. Seki, T. Nishiyama, R. Kataoka, K. Asamura, Y. Katoh, Y. Ebihara, T. Sakanoi, M. Hirahara, S. Oyama, S. Kurita, and O. Santolik (2015b), Relation between fine structure of energy spectra for pulsating aurora electrons and frequency spectra of whistler mode chorus waves, *Journal of Geophysical Research: Space Physics*, *120*(9), 7728–7736, doi:https://doi.org/10.1002/2015JA021562.

Miyoshi, Y., I. Shinohara, T. Takashima, K. Asamura, N. Higashio, T. Mitani, S. Kasahara, S. Yokota, Y. Kazama, S. Wang, S. W. Y. Tam, P. T. P. Ho, Y. Kasahara, Y. Kasaba, S. Yagitani, A. Matsuoka, H. Kojima, Y. Katoh, K. Shiokawa, and K. Seki (2018a), Geospace exploration project ERG, *Earth, Planets and Space*, *70*(1880-5981), 101, doi:https://doi.org/10.1186/s40623-018-0862-0.

Miyoshi, Y., T. Hori, M. Shoji, M. Teramoto, T. F. Chang, T. Segawa, N. Umemura, S. Matsuda, S. Kurita, K. Keika, Y. Miyashita, K. Seki, Y. Tanaka, N. Nishitani, S. Kasahara, S. Yokota, A. Matsuoka, Y. Kasahara, K. Asamura, T. Takashima, and I. Shinohara (2018b), The ERG science center, *Earth, Planets and Space*, *70*(1880-5981), 96, doi:https://doi.org/10.1186/s40623-018-0867-8.

Miyoshi, Y., S. Saito, S. Kurita, K. Asamura, K. Hosokawa, T. Sakanoi, T. Mitani, Y. Ogawa, S. Oyama, F. Tsuchiya, S. L. Jones, A. N. Jaynes, and J. B. Blake (2020), Relativistic electron microbursts as high-energy tail of pulsating aurora electrons, *Geophysical Research Letters*, *47*(21), e2020GL090,360, doi:https://doi.org/10.1029/2020GL090360.

Miyoshi, Y., K. Hosokawa, and S. e. a. Kurita (2021), Penetration of MeV electrons into the mesosphere accompanying pulsating aurorae, *Scientific Reports*, *11*, 13,724, doi:https://doi.org/10.1038/s41598-021-92611-3.

Morley, S. K., S. T. Ables, M. D. Sciffer, and B. J. Fraser (2009), Multipoint observations of Pc1-2 waves in the afternoon sector, *Journal of Geophysical Research: Space Physics*, *114*(A9), doi:10.1029/2009JA014162.

Newell, P. T., K. Liou, and G. R. Wilson (2009), Polar cap particle precipitation and aurora: Review and commentary, *J. Atmos. Terr. Phys.*, *71*, 199–215.

Ni, B., R. M. Thorne, Y. Y. Shprits, and J. Bortnik (2008), Resonant scattering of plasma sheet electrons by whistler-mode chorus: Contribution to diffuse auroral precipitation, *Geophysical Research Letters*, *35*(11), doi:https://doi.org/10.1029/2008GL034032.

Ni, B., R. M. Thorne, R. B. Horne, N. P. Meredith, Y. Y. Shprits, L. Chen, and W. Li (2011), Resonant scattering of plasma sheet electrons leading to diffuse auroral precipitation: 1.

evaluation for electrostatic electron cyclotron harmonic waves, *Journal of Geophysical Research: Space Physics*, *116*(A4), doi:https://doi.org/10.1029/2010JA016232.

Ni, B., J. Liang, R. M. Thorne, V. Angelopoulos, R. B. Horne, M. Kubyshkina, E. Spanswick, E. F. Donovan, and D. Lummerzheim (2012), Efficient diffuse auroral electron scattering by electrostatic electron cyclotron harmonic waves in the outer magnetosphere: A detailed case study, *Journal of Geophysical Research: Space Physics*, *117*(A1), doi: https://doi.org/10.1029/2011JA017095.

Ni, B., X. Cao, Z. Zou, C. Zhou, X. Gu, J. Bortnik, J. Zhang, S. Fu, Z. Zhao, R. Shi, and L. Xie (2015), Resonant scattering of outer zone relativistic electrons by multiband EMIC waves and resultant electron loss time scales, *Journal of Geophysical Research: Space Physics*, *120*(9), 7357–7373, doi:https://doi.org/10.1002/2015JA021466.

Ni, B., X. Thorne, Richard M. Zhang, J. Bortnik, Z. Pu, L. Xie, Z.-j. Hu, D. Han, R. Shi, C. Zhou, and X. Gu (2016), Origins of the earth's diffuse auroral precipitation, *Space Science Reviews*, *200*(1), 205–259, doi:10.1007/s11214-016-0234-7.

Ni, B., X. Cao, Y. Y. Shprits, D. Summers, X. Gu, S. Fu, and Y. Lou (2018), Hot plasma effects on the cyclotron-resonant pitch-angle scattering rates of radiation belt electrons due to EMIC waves, *Geophysical Research Letters*, *45*(1), 21–30, doi: https://doi.org/10.1002/2017GL076028.

Ni, B., Y. Zhang, and X. Gu (2023), Identification of ring current proton precipitation driven by scattering of electromagnetic ion cyclotron waves, *Fundamental Research*, *3*(2), 257–264, doi:https://doi.org/10.1016/j.fmre.2021.12.018.

Nishimura, L. M. K. Y. e. a., Y. (2020), Diffuse and pulsating aurora, *Space Sci. Rev.*, *4*, 216, doi:https://doi.org/10.1007/s11214-019-0629-3.

Ozaki, M., Y. Miyoshi, K. Shiokawa, K. Hosokawa, S.-i. Oyama, R. Kataoka, Y. Ebihara, Y. Ogawa, Y. Kasahara, S. Yagitani, Y. Kasaba, A. Kumamoto, F. Tsuchiya, S. Matsuda, Y. Katoh, M. Hikishima, S. Kurita, Y. Otsuka, R. C. Moore, Y. Tanaka, M. Nosé, T. Nagatsuma, N. Nishitani, A. Kadokura, M. Connors, A. Inoue, Takumi Matsuoka, and I. Shinohara (2019), Visualization of rapid electron precipitation via chorus element wave–particle interactions, *Nature Communications*, *10*, 257, doi:10.1038/s41467-018-07996-z.

P R, S., and Y. Yu (2023), SWMF simulation output [Dataset], Zenodo, doi: 10.5281/zenodo.10258540.

Popova, Y. A. G. D. A. G., T. A., and S. A. Chernyaeva (2018), Generation of EMIC waves in the magnetosphere and precipitation of energetic protons: Comparison of the data from THEMIS high earth orbiting satellites and POES low earth orbiting satellites, *Geomagnetism and Aeronomy*, *58*(4), 469–482, doi:10.1134/S0016793218040114.

Rasmussen, C. E., S. M. Guiter, and S. G. Thomas (1993), A two-dimensional model of the plasmasphere: refilling time constants, *Planetary and Space Science*, *41*(1), 35–43, doi:10.1016/0032-0633(93)90015-T.

Ridley, A. J., T. I. Gombosi, and D. L. DeZeeuw (2004), Ionospheric control of the magnetosphere: conductance, *Ann. Geophys.*, *22*, 567–584.

Saikin, A. A., J.-C. Zhang, R. C. Allen, C. W. Smith, L. M. Kistler, H. E. Spence, R. B. Torbert, C. A. Kletzing, and V. K. Jordanova (2015), The occurrence and wave properties of H^+-, He^+-, and O^+-band EMIC waves observed by the Van Allen Probes, *Journal of Geophysical Research: Space Physics*, *120*(9), 7477–7492, doi:10.1002/2015JA021358.

Saikin, A. A., J.-C. Zhang, C. W. Smith, H. E. Spence, R. B. Torbert, and C. A. Kletzing (2016), The dependence on geomagnetic conditions and solar wind dynamic pressure of the spatial distributions of EMIC waves observed by the Van Allen Probes, *Journal of Geophysical Research: Space Physics*, *121*(5), 4362–4377, doi:10.1002/2016JA022523.

Semenova, N. V., A. G. Yahnin, T. A. Yahnina, and A. G. Demekhov (2019), Properties of localized precipitation of energetic protons equatorward of the isotropic boundary, *Geophysical Research Letters*, *46*(20), 10,932–10,940, doi:10.1029/2019GL085373.

Shreedevi, P. R., S. V. Thampi, D. Chakrabarty, R. K. Choudhary, T. K. Pant, A. Bhardwaj, and S. Mukherjee (2016), On the latitudinal changes in ionospheric electrodynamics and composition based on observations over the 76-77°E meridian from both hemispheres during a geomagnetic storm, *J. Geophys. Res. Space Physics*, *121*, doi:10.1002/2015JA021841.

Shreedevi, P. R., R. K. Choudhary, Y. Yiqun, and E. G. Thomas (2019), Morphological study on the ionospheric variability at bharati, a polar cusp station in the southern hemisphere, *Journal of Atmospheric and Solar-Terrestrial Physics*, *193*, doi: https://doi.org/10.1016/j.jastp.2019.105058.

Shreedevi, P. R., R. K. Choudhary, S. V. Thampi, S. Yadav, T. K. Pant, Y. Yu, R. McGranaghan, E. G. Thomas, A. Bhardwaj, and A. K. Sinha (2020), Geomagnetic storm-induced plasma density enhancements in the southern polar ionospheric region: A comparative study using St. Patrick's day storms of 2013 and 2015, *Space Weather*, *18*(8), e2019SW002,383, doi:https://doi.org/10.1029/2019SW002383.

Shreedevi, P. R., Y. Yu, B. Ni, A. Saikin, and V. K. Jordanova (2021), Simulating the ion precipitation from the inner magnetosphere by H-band and He-band electro magnetic ion cyclotron waves, *Journal of Geophysical Research: Space Physics*, *126*(3), e2020JA028,553, doi:https://doi.org/10.1029/2020JA028553, e2020JA028553 2020JA028553.

Soraas, F., J. Lundblad, N. Maltseva, V. Troitskaya, and V. Selivanov (1980), A comparison between simultaneous I.P.D.P. groundbased observations and observations of energetic protons obtained by satellites, *Planetary and Space Science*, *28*(4), 387–405, doi: 10.1016/0032-0633(80)90043-4.

Soraas, F., K. Aarsnes, J. Lundblad, and D. Evans (1999), Enhanced pitch angle scattering of protons at mid-latitudes during geomagnetic storms, *Physics and Chemistry of the Earth, Part C: Solar, Terrestrial and Planetary Science*, *24*(1), 287 – 292, doi: https://doi.org/10.1016/S1464-1917(98)00041-5.

Spence, R. G. B. D. e. a., H.E. (2013), Science goals and overview of the radiation belt storm probes (RBSP) energetic particle, composition, and thermal plasma (ECT) suite on NASA's Van Allen Probes mission, *Space Science Reviews*, *178*, 311–336, doi: https://doi.org/10.1007/s11214-013-0007-5.

Su, Z., H. Zheng, L. Chen, and S. Wang (2011), Numerical simulations of storm-time outer radiation belt dynamics by wave–particle interactions including cross diffusion, *Journal of Atmospheric and Solar-Terrestrial Physics*, *73*(1), 95–105, doi: https://doi.org/10.1016/j.jastp.2009.08.002.

Thorne, N. B. T. X. e. a., R. (2010), Scattering by chorus waves as the dominant cause of diffuse auroral precipitation, *Nature*, *467*, 943–946, doi: https://doi.org/10.1038/nature09467.

Tian, X., Y. Yu, and C. Yue (2020), Statistical survey of storm-time energetic particle precipitation, *Journal of Atmospheric and Solar-Terrestrial Physics*, *199*(1364-6826), 105,204, doi:10.1016/j.jastp.2020.105204.

Tian, X., Y. Yu, M. Zhu, L. Ma, J. Cao, S. PR, V. K. Jordanova, and S. C. Solomon (2022), Effects of EMIC wave-driven proton precipitation on the ionosphere, *Journal of Geophysical Research: Space Physics*, *127*(2), e2021JA030,101, doi: https://doi.org/10.1029/2021JA030101.

Tian, X., Y. Yu, F. Gong, L. Ma, J. Cao, S. C. Solomon, P. R. Shreedevi, K. Shiokawa, Y. Otsuka, S.-i. Oyama, and Y. Miyoshi (2023), Ionospheric modulation by EMIC wave-driven proton precipitation: Observations and simulations, *Journal of Geophysical Research:*

Space Physics, *128*(1), e2022JA030,983, doi:https://doi.org/10.1029/2022JA030983, e2022JA030983 2022JA030983.

Usanova, M. E., I. R. Mann, J. Bortnik, L. Shao, and V. Angelopoulos (2012), THEMIS observations of electromagnetic ion cyclotron wave occurrence: Dependence on AE, SymH, and solar wind dynamic pressure, *Journal of Geophysical Research: Space Physics*, *117*(A10), doi:10.1029/2012JA018049.

Usanova, M. E., I. R. Mann, and F. Darrouzet (2016), *EMIC Waves in the Inner Magnetosphere*, chap. 5, pp. 65–78, American Geophysical Union (AGU), doi: https://doi.org/10.1002/9781119055006.ch5.

Verronen, P. T., A. Kero, N. Partamies, M. E. Szelag, S.-I. Oyama, Y. Miyoshi, and E. Turunen (2021), Simulated seasonal impact on middle atmospheric ozone from high-energy electron precipitation related to pulsating aurorae, *Annales Geophysicae*, *39*(5), 883–897, doi:10.5194/angeo-39-883-2021.

Welling, D. T., G. Toth, V. K. Jordanova, and Y. Yu (2018), Integration of RAM-SCB into the space weather modeling framework, *Journal of Atmospheric and Solar-Terrestrial Physics*, *177*, 160–168, doi:https://doi.org/10.1016/j.jastp.2018.01.007.

Xiao, F., Z. Su, H. Zheng, and S. Wang (2009), Modeling of outer radiation belt electrons by multidimensional diffusion process, *Journal of Geophysical Research: Space Physics*, *114*(A3), doi:https://doi.org/10.1029/2008JA013580.

Xiao, F., Q. Zong, Z. Su, C. Yang, Z. He, Y. Wang, and Z. Gao (2013), Determining the mechanism of cusp proton aurora, *Scientific Reports*, *3*, 1654, doi:10.1038/srep01654.

Yahnin, Y. T. A. S. N. V. P. T. A., A. G., and A. G. Demekhov (2018), Proton auroras equatorward of the oval as a manifestation of the ion-cyclotron instability in the earth's magnetosphere (brief review), *Geomagnetism and Aeronomy*, *58*(5), 577–585, doi: 10.1134/S001679321805016X.

Yahnina, T. A., A. G. Yahnin, J. Kangas, J. Manninen, D. S. Evans, A. G. Demekhov, V. Y. Trakhtengerts, M. F. Thomsen, G. D. Reeves, and B. B. Gvozdevsky (2003), Energetic particle counterparts for geomagnetic pulsations of Pc1 and IPDP types, *Annales Geophysicae*, *21*(12), 2281–2292, doi:10.5194/angeo-21-2281-2003.

Yang, Q., S. Liu, H. Yang, S. Zhang, J. Tang, F. Xiao, Q. Zhou, Z. Gao, Y. He, Z. Deng, and P. Li (2023), Efficient scattering loss of energetic electrons by enhanced higher-band ech waves observed by van allen probes, *Geophysical Research Letters*, *50*(9), e2023GL103,927, doi:https://doi.org/10.1029/2023GL103927.

Yokota, K. S. M. T. e. a., S. (2017), Medium-energy particle experiments–ion mass analyzer (MEP-i) onboard ERG (Arase), *Earth Planets Space*, *69*, 172, doi: https://doi.org/10.1186/s40623-017-0754-8.

Yokota, S., S. Kasahara, and T. Hori (2019), Exploration of energization and Radiation in Geospace (ERG) MEP-i Level-2 omni-directional flux data [Dataset], ERG Science Center, Institute for Space-Earth Environmental Research, Nagoya University, doi: 10.34515/DATA.ERG-03001.

Yu, X., Z. Yuan, S. Huang, D. Wang, H. Li, Z. Qiao, and F. Yao (2017), EMIC waves covering wide L shells: MMS and Van Allen Probes observations, *Journal of Geophysical Research: Space Physics*, *122*(7), 7387–7395, doi:10.1002/2017JA023982.

Yu, Y., V. Jordanova, S. Zou, R. Heelis, M. Ruohoniemi, and J. Wygant (2015), Modeling subauroral polarization streams during the 17 March 2013 storm, *J. Geophys. Res.*, *120*, 1738–1750, doi:10.1002/2014JA020371.

Yu, Y., X. Tian, and V. K. Jordanova (2020), The effects of field line curvature (FLC) scattering on ring current dynamics and isotropic boundary, *Journal of Geophysical Research: Space Physics*, *125*(8), e2020JA027,830, doi:https://doi.org/10.1029/2020JA027830.

Yu, Y., K. Hosokawa, B. Ni, V. K. Jordanova, Y. Miyoshi, J. Cao, X. Tian, and L. Ma (2022), On the importance of using event-specific wave diffusion rates in modeling diffuse electron precipitation, *Journal of Geophysical Research: Space Physics*, *127*(4), e2021JA029,918, doi:https://doi.org/10.1029/2021JA029918, e2021JA029918 2021JA029918.

Zaharia, S., V. K. Jordanova, M. F. Thomsen, and G. D. Reeves (2006), Self-consistent modeling of magnetic fields and plasmas in the inner magnetosphere: Application to a geomagnetic storm, *Journal of Geophysical Research: Space Physics*, *111*(A11), doi: 10.1029/2006JA011619, a11S14.

Zhang, X.-J., V. Angelopoulos, B. Ni, and R. M. Thorne (2015), Predominance of ECH wave contribution to diffuse aurora in earth's outer magnetosphere, *Journal of Geophysical Research: Space Physics*, *120*(1), 295–309, doi:https://doi.org/10.1002/2014JA020455.

Zhu, M., Y. Yu, X. Tian, P. R. Shreedevi, and V. K. Jordanova (2021a), On the ion precipitation due to field line curvature (FLC) and EMIC wave scattering and their subsequent impact on ionospheric electrodynamics, *Journal of Geophysical Research: Space Physics*, *126*(3), e2020JA028,812, doi:https://doi.org/10.1029/2020JA028812, e2020JA028812 2020JA028812.

Zhu, M., Y. Yu, and V. K. Jordanova (2021b), Simulating the effects of warm O+ ions on the growth of electromagnetic ion cyclotron (EMIC) waves, *Journal of Atmospheric and Solar-Terrestrial Physics*, *224*, 105,737, doi:https://doi.org/10.1016/j.jastp.2021.105737.

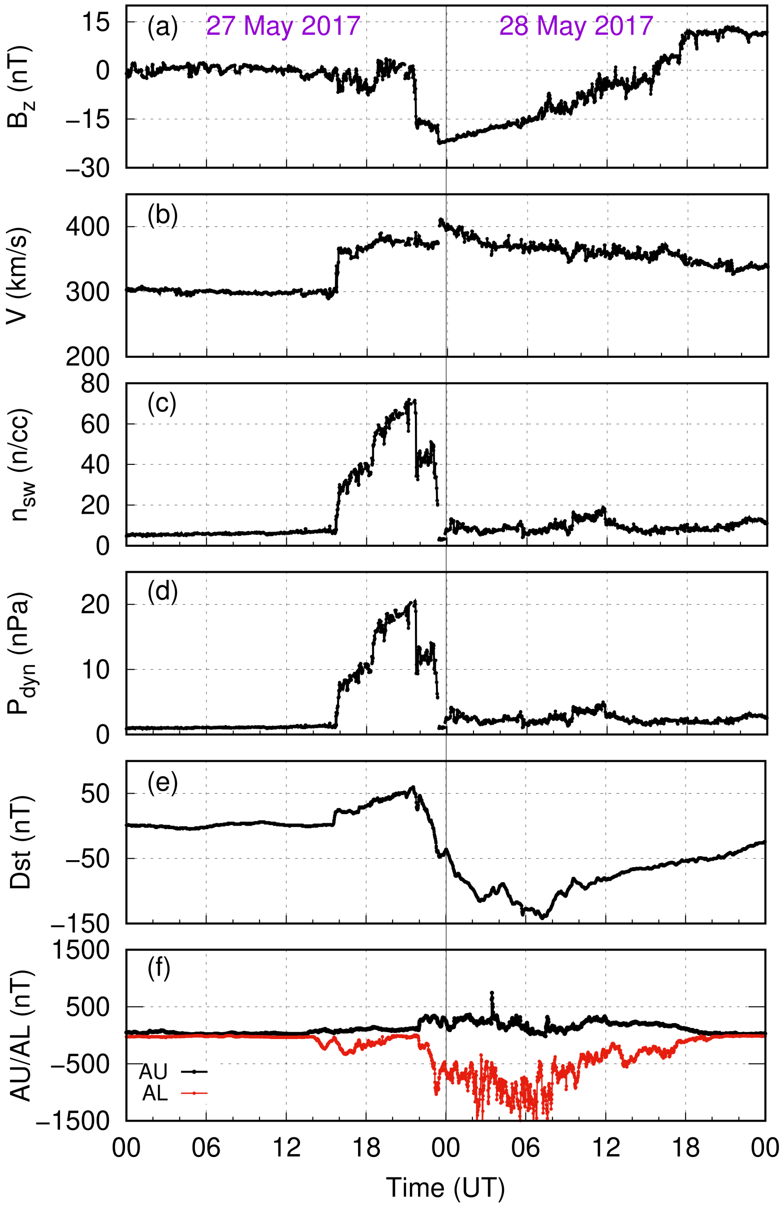

Figure 1. Solar wind and geomagnetic conditions during 27 May 2017: Panels (a-f) show the variation of (a) IMFB_z, (b) solar wind speed (c) solar wind density, (d) solar wind dynamic pressure, (e) Dst index, (f) AU/AL index

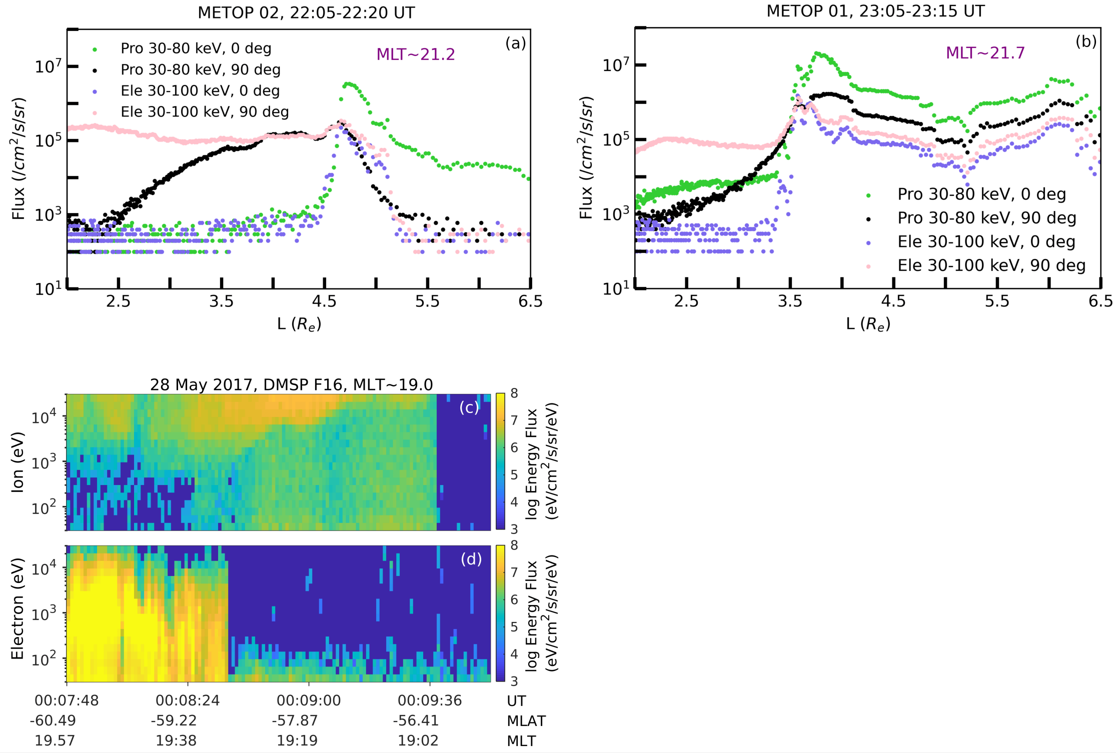

Figure 2. Satellite observations of particle precipitation during 27 May 2017: Panel (a, b) shows the 30-80 keV proton and 30-100 keV electron precipitation flux observed by the NOAA/MetOp 01 and 02 satellites, respectively, and Panel (c, d) shows the comparison of the DMSP F16 energy spectrogram of ions and electrons, respectively.

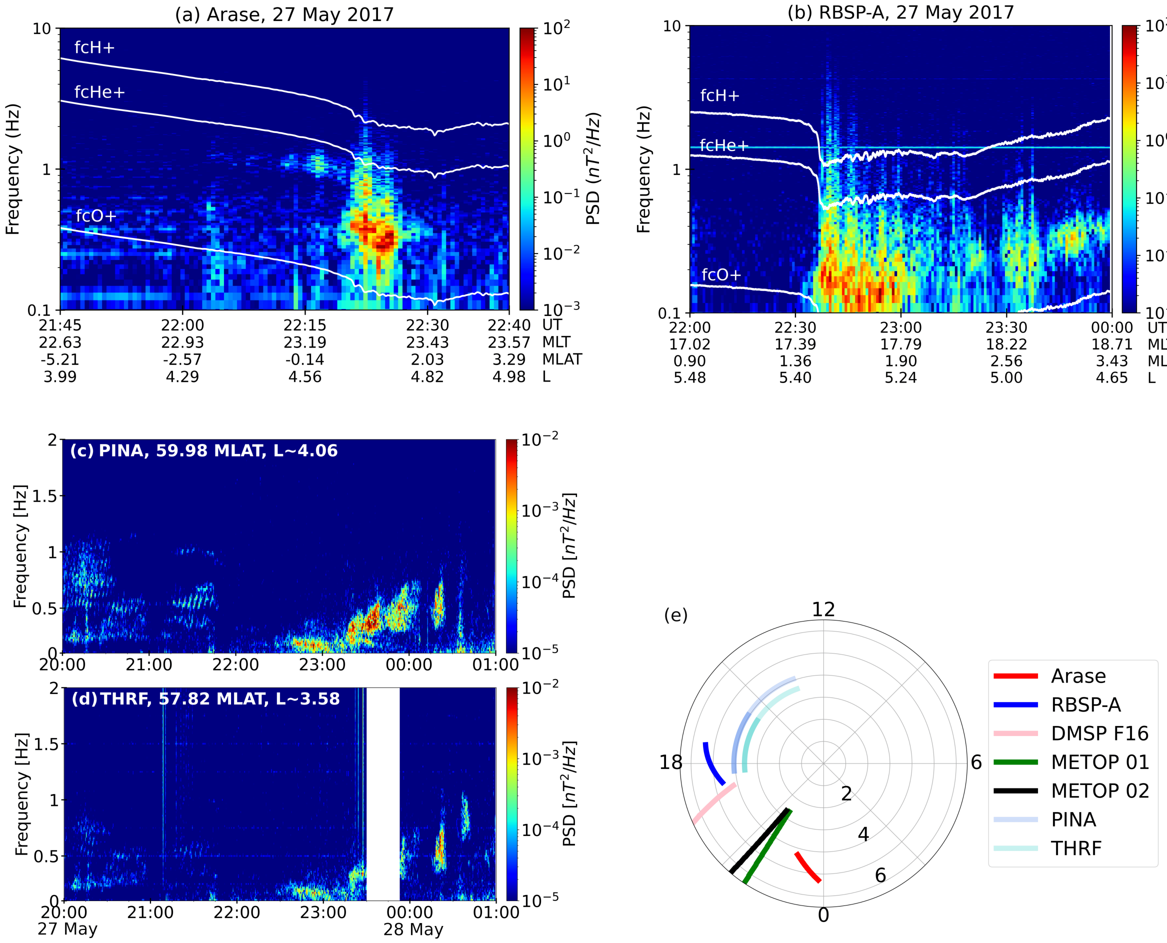

Figure 3. Space/ ground-based observations of the EMIC wave activity during 27 May 2017: Panels (a, b) shows the power spectral density (PSD) of the magnetic field measured by the Arase and RBSP-A satellites, respectively. Panels (c, d) shows the variation of PSD at Pinawa (PINA) and Thief River Falls (THRF) during 2000 UT on 27 May to 0100 UT on 28 May. The white lines on the spectrogram indicate the local H^+, He^+ and O^+ ion gyrofrequencies. Panel (e) shows the location of all space/ground-based observations during the interval 2200 on 27 May to 0100 UT on 28 May in the L-MLT plane

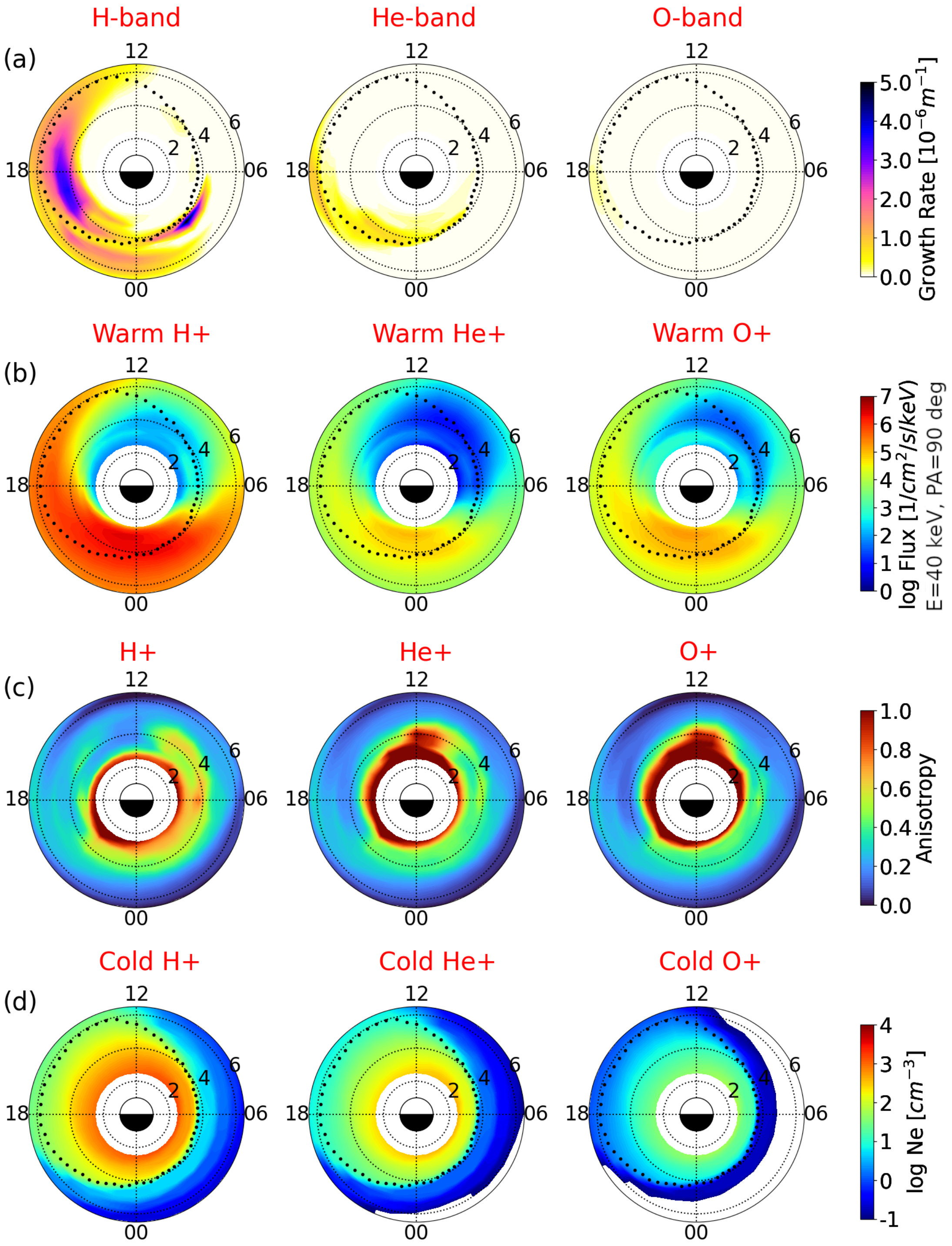

Figure 4. (a) Global distribution of the maximum growth rate of the H-band, He-band and O-band EMIC waves, (b) The anisotropy of hot H^+, He^+ and O^+ ions at 22:55 UT, (c) Fluxes of H^+, He^+ and O^+ ions at energy E=40 keV, pitch angle=90° at 22:55 UT, (d) global distribution of cold H^+, He^+ and O^+ ion density at 2215 UT

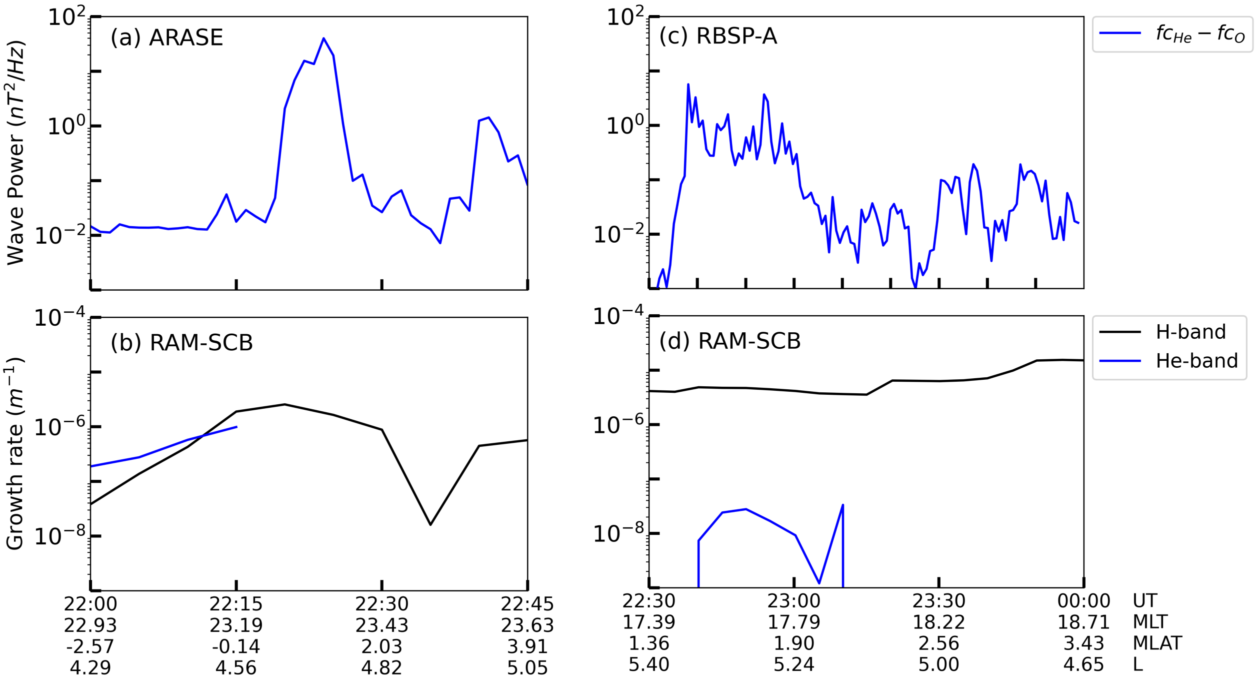

Figure 5. (a) Integrated wave power between fc_{He}-fc_O estimated from Arase observations during 2200-2245 UT on 27 May 2017, where fc_{He} and fc_O are the He^+ and O^+ local gyrofrequencies, respectively. (b) same as panel (a), but for RBSP-A observations. (c) Variation of maximum growth rate of H- and He-band EMIC wave along the Arase satellite orbit. (d) same as panel (c), but for RBSP-A satellite.

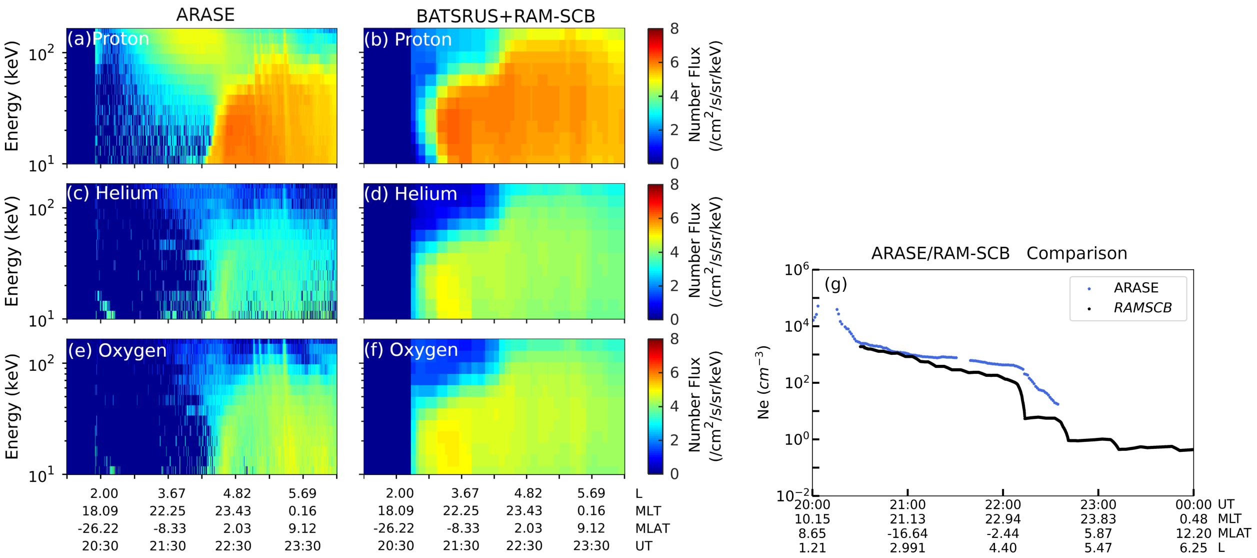

Figure 6. Panels (a, c, e) show energy-time diagram of the 10-180 keV proton, helium and oxygen fluxes measured by the Arase satellite during 2000-2400 UT on 27 May 2017. Panels (b, d, f) show energy-time diagram of the simulated 10-180 keV proton, helium and oxygen fluxes during 2000-2400 UT on 27 May 2017. (g) Comparison of the cold plasma density (Ne) obtained from RAM-SCB simulation with EMIC waves and that observed by the Arase satellite.

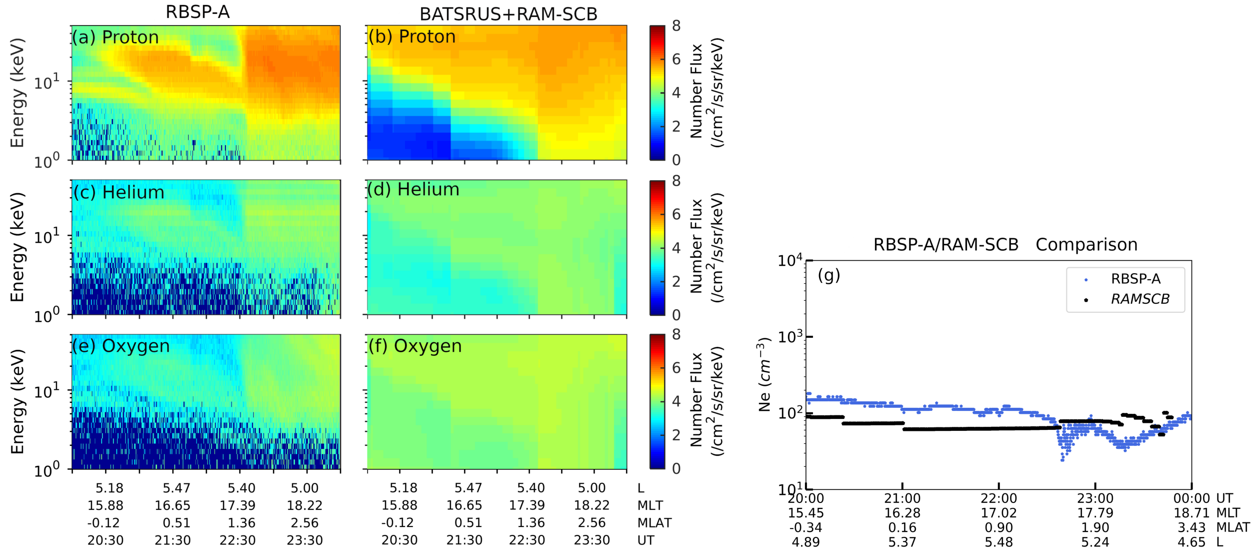

Figure 7. Panels (a, c, e) show energy-time diagram of the 1-50 keV proton, helium and oxygen fluxes measured by the RBSP-A satellite during 2000-2400 UT on 27 May 2017. Panels (b, d, f) show energy-time diagram of the simulated 1-50 keV proton, helium and oxygen fluxes during 2000-2400 UT on 27 May 2017. (g) Comparison of the cold plasma density (Ne) obtained from RAM-SCB simulation with EMIC waves and that observed by the RBSP-A satellite.

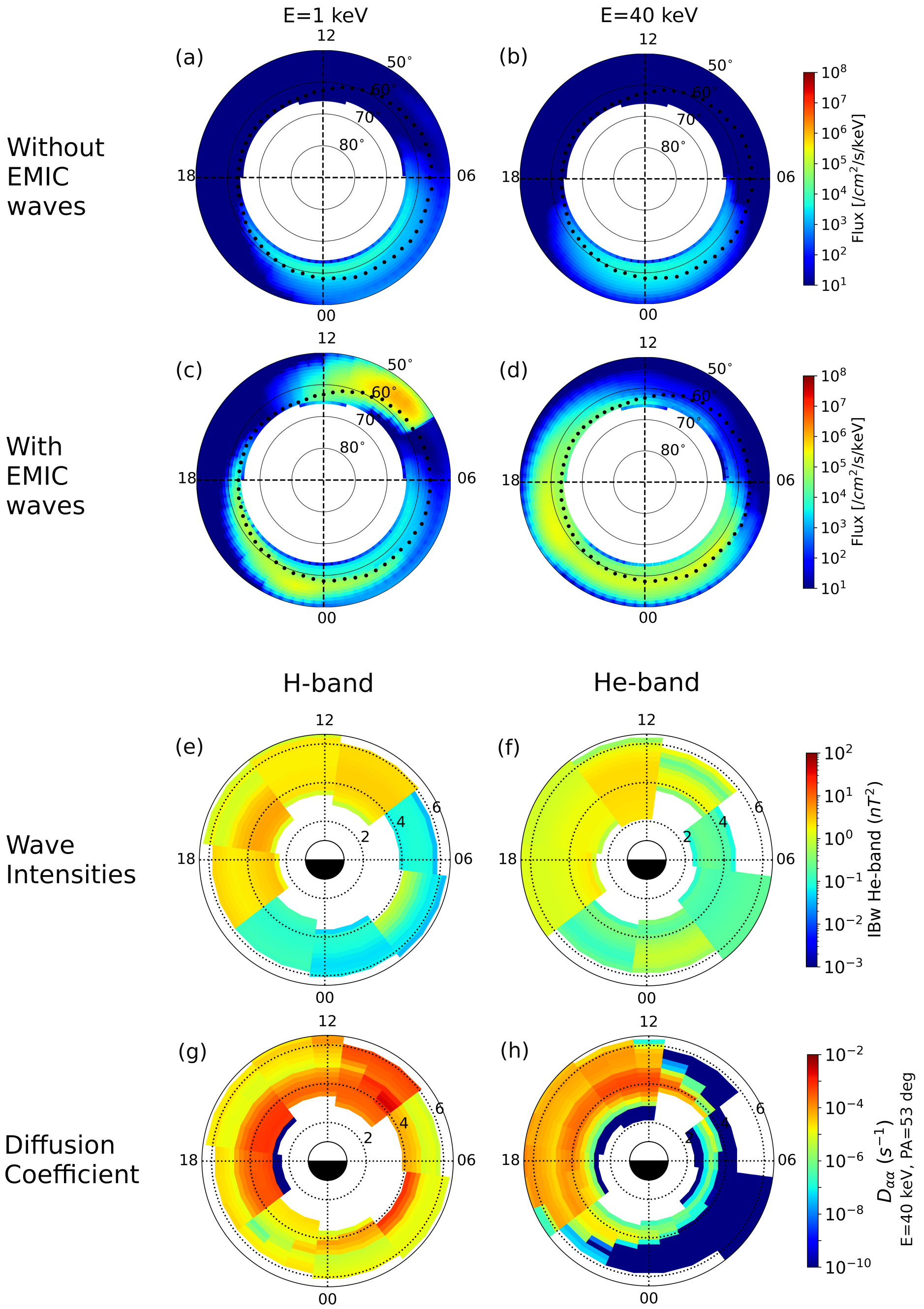

Figure 8. Panels(a, b) show the distribution of precipitating proton fluxes in the equatorial plane at ionospheric altitudes from the simulations with EMIC waves. Panels(c, d) show the precipitating proton fluxes from the simulations without EMIC waves. Panels (e, f) show the distribution of the H- and He-band EMIC wave magnetic field density (IB_w). Panels (g, h) show the distribution of diffusion coefficients due to H- and He-band EMIC waves. The diffusion coefficients are those for protons with E = 40 keV and pitch angle 53 deg. All the plots are chosen at 2215 UT on 27 May 2017.

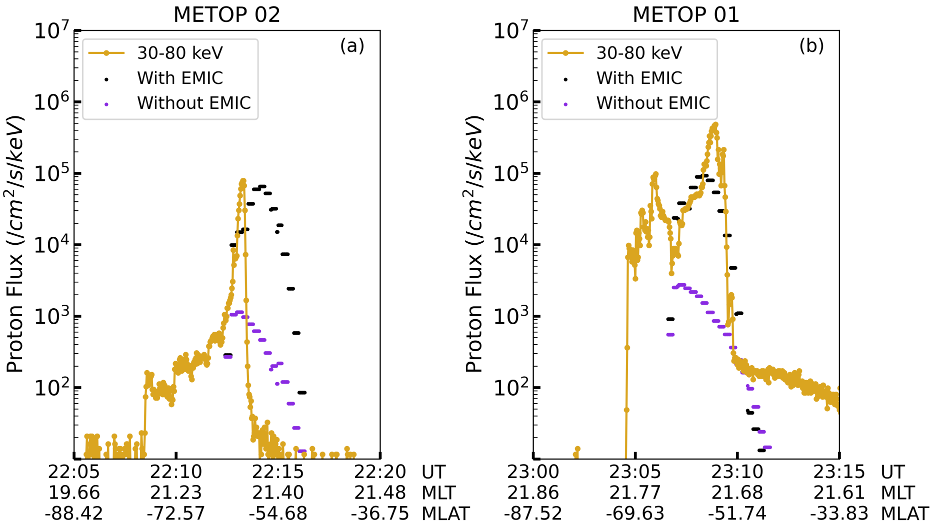

1244 **Figure 9.** Panels (a, b) show the comparison between the 30-80 keV precipitating proton fluxes
1245 obtained from NOAA MetOp 01 and 02 satellite and the RAM-SCB simulations with and without
1246 EMIC waves.

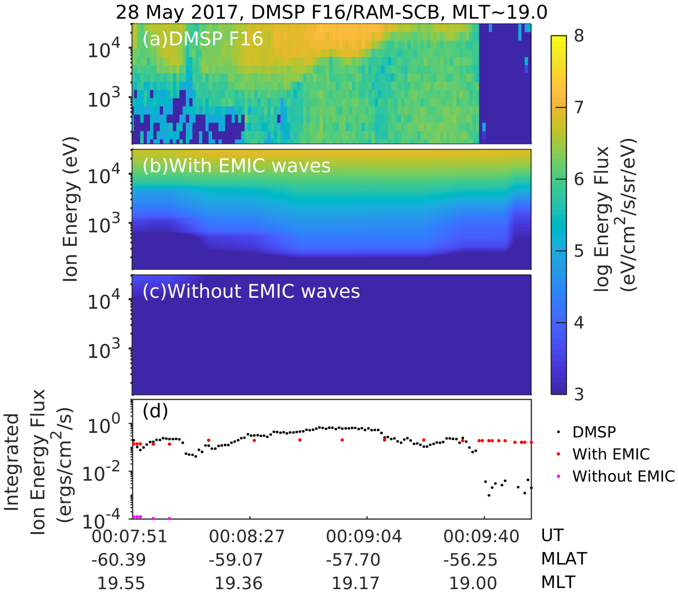

Figure 10. Comparison between DMSP F16 satellite measurements and the RAM-SCB simulations with and without EMIC waves for 27 May 2017: Panel (a) shows the DMSP F16 energy spectrogram of ions in log scale. Panels (b, c) shows the energy spectrogram of ions from simulations. Panel (d) shows the comparison of integrated ion energy flux from DMSP observations with the two RAM-SCB simulations.